Spring 2020

Influence of Dynamic Multiaxial Transverse Loading on Ultrahigh Molecular Weight Polyethylene Single Fiber Failure

Frank David Thomas

INFLUENCE OF DYNAMIC MULTIAXIAL TRANSVERSE LOADING ON ULTRAHIGH MOLECULAR WEIGHT POLYETHYLENE SINGLE FIBER FAILURE

by

Frank David Thomas

Bachelor of Science
University of South Carolina, 2017

Submitted in Partial Fulfillment of the Requirements

For the Degree of Master of Science in

Mechanical Engineering

College of Engineering and Computing

University of South Carolina

2020

Accepted by:

Subramani Sockalingam, Director of Thesis

Tusit Weerasooriya, Reader

Cheryl L. Addy, Vice Provost and Dean of the Graduate School

ACKNOWLEDGEMENTS

Research funding for the author was sponsored by the Oak Ridge Institute for Science and Education, which is managed by Oak Ridge Associated Universities. Equipment, facilities, and training were provided by the Army Research Laboratory at Aberdeen Proving Ground, Maryland. Procedural design and initial experimentation for fiber residual strength is performed by Mr. Elvis Budelkhandi of the University of South Carolina. Preliminary experimentation for single fiber impact is performed by Mr. Robert Bass of the University of South Carolina. The views and conclusions contained in this document are those of the authors and should not be interpreted as representing the official policies, either expressed or implied, of the Army Research Laboratory or the U.S. Government. The U.S. Government is authorized to reproduce and distribute reprints for Government purposes notwithstanding any copyright notation herein.

The author would like to acknowledge Drs. Tusit Weerasooriya and Allan Gunnarsson, and Mr. Stephen Alexander of Army Research Laboratory at Aberdeen Proving Ground, Maryland for their support with both administrative and technical concerns throughout the projects. Additionally, the author would like to acknowledge Dr. Subramani Sockalingam for his guidance and patience in the development of this thesis.

ABSTRACT

High performance fibers such as ultrahigh molecular weight polyethylene (UHMWPE) are often used for ballistic impact applications in the form of textile fabrics and composite laminates. In order to predict the ballistic performance of such materials, single-fiber experiments are performed to quantify the material behavior at smaller length scales, which can be applied to larger length scales as a result. Failure of UHMWPE is well understood as a function of simple tension at low and high strain rates, as well as under various multiaxial loading states. However, experimental characterization of single UHMWPE fibers under transverse loading at high strain rates (4000-7000 s^{-1}) has not yet been performed due to the lack of available methodology.

In this work, a single fiber transverse impact experimental technique is developed at the Army Research Laboratory (ARL) labs. A small-diameter Hopkinson bar is modified to launch custom-designed loading geometries on individual fibers mounted transversely to the path of motion. Load cells at the grips record forces experienced by the fiber, and a high framerate camera captures the test progression and deformation behavior. Loading geometries are all circular with varying radius including a razor (~2 μm), a sharp indenter (20 μm), and a blunt indenter (200 μm), and two impact velocities are chosen, 10 m/s and 20 m/s, which correlate to strain rates of approximately 4320 and 6846 s^{-1}.

This novel apparatus and experimental design is used to study the transverse impact behavior of UHMWPE Dyneema® SK76 single fibers with average diameters of 17 um. Failure strain for all groups is significantly reduced relative to existing tensile and quasi-

static (QS) transverse loading data. For all the geometries, failure strains are reduced by 46-51%, compared to QS tensile and 12-19% compared to QS transverse, as strain rates increased from 4320-6846 s^{-1}. Compared to high strain rate (1156 s^{-1}) tensile failure strain, significant reduction in failure strains are measured due to transverse impact loading. Failure strains (i) reduced by 28-34% for blunt impact at strain rates 4369-6952 s^{-1}; (ii) reduced by 32-39% for sharp impact at strain rates 4285-6797 s^{-1} and (iii) reduced by 58-61% for razor impact at strain rates 4307-6789 s^{-1}. For all the geometries, change in strength ranges from +6% to -2%, compared to QS tensile, as strain rates increased from 4320-6846 s^{-1}. Compared to high strain rate tensile strength, changes in strength can range from a slight increase to a significant reduction due to interactions between the rate-dependent increases in stiffness and strength, and strength degradation due to transverse loading. Strength measurements (i) range from +6% to -2% for blunt impact at strain rates 4369-6952 s^{-1}; (ii) range from +4% to -8% for sharp impact at strain rates 4285-6797 s^{-1} and (iii) range from -28% to -42% for razor impact at strain rates 4307-6789 s^{-1}. The reduction in tensile properties are attributed to the failure mechanism induced by different geometries. While all geometries induce axial compression due to the impact, the loading radius affects the degree of applied transverse shear, where little to no transverse shear is observed in the blunt indenter, an intermediate amount of shear is applied in the sharp indenter, and a high degree of shear is applied by the razor indenter. This conclusion is supported by failure surface images, where blunt impact results in fibrillation characteristic of tensile failure, razor impact results in fiber shearing characteristic of the cutting action of the razor, and the sharp impact demonstrates a mixed amount of both failure modes.

The experiments are modeled in LS-DYNA using a custom user material model (UMAT) to incorporate nonlinear inelastic transverse compressive behavior. Model predictions correlate well to the experimental observations in terms of load and strain values as well as in qualitative characterization of the material response to impact loading. A previously-developed strain-based single fiber multiaxial failure criterion is discussed and applied to the model output, but more development is necessary for this criterion to have predictive capabilities for high strain rate impact of UHMWPE.

TABLE OF CONTENTS

ACKNOWLEDGEMENTS III

ABSTRACT IV

TABLE OF CONTENTS VII

LIST OF TABLES IX

LIST OF FIGURES X

LIST OF ABBREVIATIONS XIII

CHAPTER 1 INTRODUCTION 1

1.1 MULTISCALE MECHANICS OF MATERIALS OVERVIEW 1

1.2 RESEARCH OBJECTIVES 3

1.3 THESIS OUTLINE 4

CHAPTER 2 LITERATURE REVIEW 5

2.1 TRANSVERSE IMPACT OF FABRICS AND YARNS 5

2.2 TENSILE PROPERTIES OF DYNEEMA® SK76 8

2.3 MULTIAXIAL LOADING OF SINGLE FIBERS 12

2.4 SUMMARY 20

CHAPTER 3 INFLUENCE OF HIGH STRAIN RATE TRANSVERSE COMPRESSION ON THE TENSILE STRENGTH OF UHMWPE SINGLE FIBERS 22

3.1 METHODS 22

3.2 RESULTS AND DISCUSSION 25

3.3 SUMMARY 31

CHAPTER 4 EXPERIMENTAL DESIGN FOR SINGLE FIBER TRANSVERSE IMPACT 32

4.1 METHODS 32

4.2 RESULTS AND DISCUSSION 38

4.3 SUMMARY 50

CHAPTER 5 FINITE ELEMENT APPROACH FOR SINGLE FIBER IMPACT 52
5.1 ORTHOTROPIC MODEL DESIGN 52
5.2 UMAT APPLICATION 55
5.3 EXPERIMENTAL CORRELATION 55
CHAPTER 6 CONCLUSIONS AND FUTURE WORK 68
REFERENCES 71

LIST OF TABLES

Table 3.1 Weibull parameters based on strain rate and damage 30

Table 4.1 Experimental Data Summary 44

Table 4.2 Average and analytically determined properties 47

Table 5.1 Initial input properties 54

Table 5.2 Effective E_3 values used in models 56

Table 5.3 Failure criterion inputs 65

LIST OF FIGURES

Figure 1.1 (a) Chemical formula for UHMWPE. (b) Ballistic helmet produced using UHMWPE [3] 3

Figure 2.1 Smith theory of transverse fiber impact 6

Figure 2.2 Effects of strain rate and gage length on (a) failure strain and (b) strength [11] 10

Figure 2.3 (a) Scanning electron micrograph of fracture site in ±45° UHMWPE laminate. (b) High-rate yarn testing apparatus 11

Figure 2.4 Initial modulus measurements for high-rate yarn loading in Russell et al. [12] 12

Figure 2.5 (a) Fiber model transversely loaded. (b) Maximum axial tensile strain evolution with stress concentration factor for 32° failure angle. (c) Comparison of failure strain as a function of failure angle. 14

Figure 2.6 Gage length-dependent axial tensile failure strain for Dyneema® SK76 UHMWPE fiber 15

Figure 2.7 (a) Apparatus for applying torque to single fibers. (b) Biaxial shear/tension failure surface [20] 16

Figure 2.8 Radius of curvature measurements for (a) FSP and (b) razor cross-sections [21] 18

Figure 2.9 Experimental setup for QS transverse loading. (a) Indenter geometries from left to right: FSP, round, razor. (b) Test schematic for single fiber transverse loading [21] 19

Figure 2.10 Scanning electron micrographs of fiber failure surface. From left to right: razor, FSP, round [21] 19

Figure 2.11 Failure strain correlated with angle of failure [21] 20

Figure 3.1 Schematic of single fiber HSR transverse compression (not to scale) 23

Figure 3.2 Single fiber window frame 24

Figure 3.3 Schematics of single fiber tensile apparatus. (a) Psylotech nTs for QS tests. (b) Hopkinson bar for HSR tests. 25

Figure 3.4 Nominal stress strain behavior in compressive loading of Dyneema SK76. .. 26

Figure 3.5 Confocal microscopy image of Dyneema SK76 at 54,117 1/s to 70% nominal strain. 26

Figure 3.6 Nominal stress-strain of representative samples. (a) HSR (~1000 1/s strain rate). (b) QS (0.001 1/s strain rate). Nominal area is original fiber area, and nominal gauge length is 10mm. 28

Figure 3.7 Mean maximum stress with 95% confidence intervals. Uncompressed (UC) sample values based on [11]. Compressed (C) sample values from experimental data. .. 29

Figure 3.8 Weibull probability plots for uncompressed (UC) and compressed (C) fibers for each strain rate. (a) HSR (~1000 1/s strain rate). (b) QS (0.001 1/s strain rate).. 30

Figure 4.1 Schematic and image of experimental apparatus for single fiber transverse impact 34

Figure 4.2 Nylon sleeve with indenter 34

Figure 4.3 Comparison of indenter geometries 36

Figure 4.4 Microscope image of blunt indenter tip 37

Figure 4.5 Representative load cell traces for (a) 10 m/s impact velocity (4295-4380 s^{-1} approximate strain rate) and (b) 20 m/s impact velocity (6805-6968 s^{-1} approximate strain rate) 39

Figure 4.6 Experimental image analysis. (a) Progressive loading of single fiber. Images range from undeformed state (far left) to final ultimate tensile strain before failure (far right). (b) Angle measurement in final frame before failure. (c) Fiber motion post-failure. 39

Figure 4.7 Experimental velocity comparison 40

Figure 4.8 Average strength comparison with standard deviation 42

Figure 4.9 Average strain comparison with standard deviation 43

Figure 4.10 Strain as a function of failure angle. Additional data is from [11] and [21]. Horizontal lines represent tensile values, and values in box are from high-rate transverse impact. 45

Figure 4.11 Transverse wave velocity and initial wave angle as a function of impact velocity 46

Figure 4.12 Broken fiber ends for each experimental case: (a) Blunt, 6951 s^{-1}; (b) Blunt, 4369 s^{-1}; (c) Sharp, 6797 s^{-1}; (d) Sharp, 4285 s^{-1}; (e) Razor, 6789 s^{-1}; (f) Razor, 4307 s^{-1}50

Figure 5.1 Front and side view of mesh for each model. From top to bottom: blunt, sharp, razor 53

Figure 5.2 UMAT behavior under transverse compression [25] 55

Figure 5.3 Model outputs correlated to analytical and experimental data for blunt, 6951 s^{-1} tests: (a) wave angle and (b) load cell data..... 57

Figure 5.4 Axial strain contours for (a) front and (b) back surfaces of fiber impacted by blunt projectile at 20 m/s..... 58

Figure 5.5 Axial strain contours for (a) front and (b) back surfaces of fiber impacted by sharp projectile at 20 m/s 59

Figure 5.6 Axial strain contours for (a) front and (b) back surfaces of fiber impacted by razor projectile at 20 m/s..... 60

Figure 5.7 Transverse compression contours for (a) blunt, (b) sharp, and (c) razor indenters at 20 m/s 62

Figure 5.8 Transverse shear contours for (a) blunt, (b) sharp, and (c) razor indenters at 20 m/s..... 63

Figure 5.9 Strain values for use in failure criterion compared to experimental data..... 65

Figure 5.10 Failure criterion components for the sharp indenter at 6797 s^{-1}. (a) Maximum axial strain and strain concentration factor. (b) Transverse compressive and shear strains. Transverse compression is equivalent across all geometries, and transverse shear is comparable across strain rates. 66

Figure 5.11 Failure criterion plots for all test groups 67

LIST OF ABBREVIATIONS

AC ..... Axial Compression

FSP ..... Fragment-Simulating Projectile

HSR ..... High Strain Rate

PMMA ..... Polymethyl Methacrylate

QS ..... Quasi-Static

SCF ..... Stress Concentration Factor

TC ..... Transverse Compression

TS ..... Transverse Shear

UHMWPE ..... Ultra-High Molecular Weight Polyethylene

CHAPTER 1

INTRODUCTION

1.1 MULTISCALE MECHANICS OF MATERIALS OVERVIEW

In applications requiring high material strength relative to overall weight, which range from body armor to vehicle frames, fiber-based composite systems are often an attractive choice, as many fibrous materials have significant tensile strength and can be either woven into fabric or bonded to matrix material to form solid structures with performance similar to metals at a fraction of the weight. Simple applications of composite materials can be analyzed and tested under the assumption that the material will behave as a continuous medium, but more complex attempts at optimization for particular use cases result in such assumptions yielding inaccurate predictions of behavior. In such situations, the analysis must be performed with the understanding of the heterogeneous material structure and the behaviors of constituent parts in mind. This approach is known as multiscale mechanics of materials and requires experimental knowledge of material behavior at progressively smaller length scales to quantify processing-structure-property relationships. For example, the ability to effectively model performance of a bulletproof vest first requires an accurate model of the constituent woven fabric, which in turn requires experiments done to characterize the fibrous material at both yarn and individual fiber levels. Efforts have even been made to understand single fiber structure and failure

behavior from a molecular level, which contributes to predictive capabilities on the macroscopic fiber level [1].

Progressively smaller length scales pose new challenges to experimental design in terms of both testing instrumentation and data capture, as simply gripping a single fiber can prove difficult in many cases, and the measurement of strains by any means other than displacement is all but impossible. Furthermore, for applications where an understanding of behavior under high-rate loading is necessary, the challenges of experimental design at the single fiber scale are amplified. In an effort to expand the knowledge of possible techniques that can be utilized for such a situation, this thesis presents a novel experimental process of testing single fibers under dynamic transverse impact and applies it to ultrahigh molecular weight polyethylene (UHMWPE) in the form of Dyneema® SK76, with comparisons made to results from existing testing methods.

UHMWPE fiber, a gel-spun polymer comprised of two-carbon monomer units as pictured in Figure 1.1(a) is an attractive option for many applications due to its high strength in many applications compared to conventional materials [2]. In addition to woven fabric, laminar sheets produced with the material can be molded to complex geometries through creep forming and other methods, making it useful for applications such as ballistic helmets as seen in Figure 1.1(b) [3]. Because of these advantages, quantitative predictions for the behavior of UHMWPE-based structures is a highly desirable goal for research and industry alike. Experiment-driven modeling efforts have made great strides in understanding the mechanisms controlling material failure, but some improvements must still be made to quantify the behavior of individual fibers, primarily due to the difficulty associated with performing tests at that length scale.

(a)

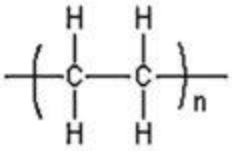

(b)

Figure 1.1 (a) Chemical formula for UHMWPE. (b) Ballistic helmet produced using UHMWPE [3]

1.2 RESEARCH OBJECTIVES

The primary objective of this research is to characterize the behavior to Dyneema® SK76 single fibers under dynamic transverse impact. To accomplish this task, several steps are necessary. First, the existing literature must be critically evaluated so that experimental data is interpreted based on the current understanding of microscale behaviors. Next, an intermediate procedure for quantifying the strength reduction due to pure transverse compression. Then, the experimental process for true transverse impact must be detailed and the resulting data analyzed. Finally, a hybrid modelling approach must be applied in order to characterize certain factors which are difficult to quantify in a purely experimental setting. All this information must be synthesized and applied to improve the predictive capabilities of composite transverse impact models on a fiber scale.

1.3 THESIS OUTLINE

This thesis will fulfill these objectives as follows:

Chapter 2 discusses research which underlies the experimental and modeling processes.

Chapter 3 details the experimental design and methodology for quantifying strength degradation due to high strain rate transverse loading.

Chapter 4 details the experimental design for single-fiber transverse impact and explains the methodology. Both strain rate and geometry are varied in order to capture various failure mechanisms and their effects on fiber strength and failure strain.

Chapter 5 applies a finite element modeling method for replicating the experimental process. Models are correlated with experimental results.

Chapter 6 concludes the thesis with a critical examination of methodology and results.

CHAPTER 2

LITERATURE REVIEW

This literature review chapter examines the existing body of literature, historic as well as current, as it relates to the performance of high-performance single fibers under multiaxial loading.

2.1 TRANSVERSE IMPACT OF FABRICS AND YARNS

Woven fabrics have long been used in armor systems for ballistic applications, so developing the understanding of the response at a material and structural level has been a major research goal as long as engineering mechanics has existed as a field of study. J. Cole et al. use the assumption of a semi-infinite elastic string impacted at a point to develop a model for transverse wave propagation [4]. While the semi-infinite string condition is not able to be replicated under experimental conditions, the assumptions underlying the model hold true at short time scales initially after impact. Based on this work, transverse wave propagation speed (c_s) can be estimated based on axial wave speed (c) and impact velocity (V) as shown in Equation 2.1, where c is calculated based axial stiffness (E) and density (ρ) as in Equation 2.2.

$$c_s = \left(\frac{c}{2}\right)^{\frac{1}{3}} (V)^{\frac{2}{3}} \tag{2.1}$$

$$c = \sqrt{\frac{E}{\rho}} \tag{2.1}$$

The work of Smith et al. is among the earliest to examine the stress-strain behavior of yarns under strain rates equivalent to ballistic impact [5]. Through multiflash photography of vertically suspended high tenacity nylon and polyester yarns transversely impacted by a 0.22 caliber rifle bullet, a V shape, which forms an angle γ from horizontal, is observed at the impact site which propagates toward the ends at a rate equivalent to the transverse wave propagation speed. A general schematic of the transverse fiber impact can be seen in Figure 2.1. Marks at regular intervals allow for the quantification of axial strain over time and the resulting axial wave speed in the material. Analytical relationships between experimental and material parameters such as impact velocity and axial wave speed, and useful quantities such as particle velocity, transverse wave speed, and axial strain are developed based on this data and are codified as the Smith theory, which is commonly applied in the first step of predicting the response of filamentous material under transverse impact. Impact velocity is related to strain by Equation 2.2, and wave angle γ is calculated based on Equation 2.3. When failure strain is inserted into the impact velocity equation, the instantaneous rupture velocity can be calculated.

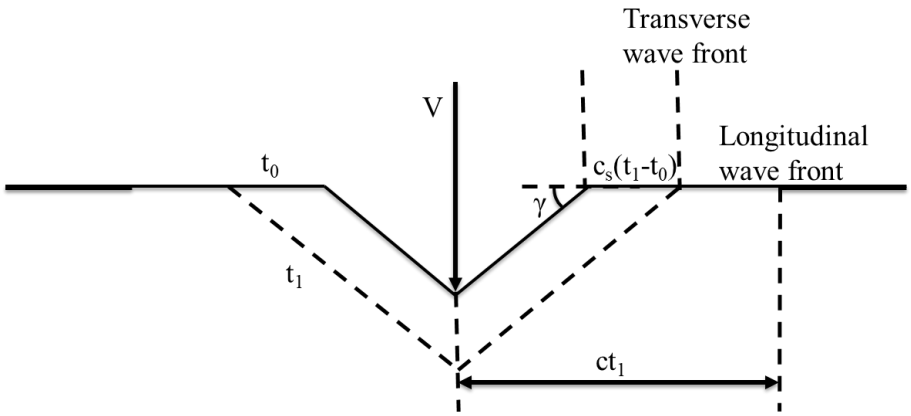

Figure 2.1 Smith theory of transverse fiber impact

$$V = c\sqrt{2\varepsilon\sqrt{\varepsilon(1+\varepsilon)} - \varepsilon^2} \tag{2.2}$$

$$\gamma = \tan^{-1}\left(\frac{2V}{c}\right)^{1/3} \tag{2.3}$$

Despite the usefulness of the Smith theory, it does have some weaknesses: First, it assumes rate-independence. Many materials have a different mechanical response depending on the applied strain rate, especially UHMWPE, so predictions may be inaccurate for such materials. Second, the Smith theory is incapable of predicting interactions of reflected waves. When a traveling wave reaches the end of a material, it will reflect back and interact with itself and any additional waves. This is mathematically difficult to quantify in terms of analytical solutions, so late-stage behavior of impacted yarns that do not rupture soon after impact cannot be described by these equations. This shortcoming is particularly bad for single-fiber applications where maintaining a longer gage length is difficult. David Roylance identifies these shortcomings and expands the theory to incorporate a rate-dependent failure criterion based on an energy-based strength prediction method [6]. This work is applied to ballistic nylon, and critical impact velocity, which is defined as the speed at which rupture occurs less than fifty milliseconds after impact, is predicted. In both of these studies, the boundary conditions for the yarn is that one end is clamped and the other is suspended by a 100 g weight, which means that if failure does not occur due to fiber rupture, stress concentrates at the clamped end, and failure occurs there.

Efforts have been made to obtain effective predictive metrics of ballistic performance based on geometry and mechanical properties. Philip Cunniff has developed a number of dimensionless parameters which generally correlate well with experimental

ballistic data [7]. This study considers UHMWPE in the form of Spectra®, but factors relating to mechanical behavior beyond stiffness and density alone result in these parameters being inaccurate metrics relative to other fiber systems such as aramid or nylon, indicating that they are mostly useful as a theoretical limit for performance.

Sánchez-Gálvez et al. have developed and validated a more complex analytical model for predicting impact performance of woven materials based on velocity and direction of impact for a round projectile [8]. Correlation with experimental data is good, which indicates that this model is effective for preliminary analysis at the fabric level.

Experimental and modeling efforts have been made to determine impact performance of materials incorporating ballistic fibers, with both woven and unidirectional ply configurations. Ruiz et al. have tested unidirectional UHMWPE material under medium velocity impact utilizing a gas gun setup and determined that orthogonal and unidirectional ply orientations are most effective at energy dissipation [9]. Vargas-Gonzalez and Gurganus have evaluated the deformation behavior of UHMWPE under ballistic impact conditions as a function of laminate architecture and have found an optimized structure which demonstrates a significantly improved response relative to a simple orthogonal laminate [10]. Hazzard et al. have performed low-velocity impact on several UHMWPE laminate designs to evaluate the effects on back face deflection, identifying laminate-level deformation mechanisms underlying this behavior.

2.2 TENSILE PROPERTIES OF DYNEEMA® SK76

UHMWPE as a material has relatively low density and does not degrade under UV light like aramid fibers, yet yarns have relatively high stiffness and tenacity, which means it is highly desirable for ballistic applications. Dyneema® SK76 has been used as a

standard application of the material for single-fiber testing due to its largely circular cross section, which makes calculating engineering stress simpler than other material systems with non-uniform cross-sectional geometry. However, traditional methods for performing single fiber testing have proven insufficient due to the tendency of the fibers to slip in the adhesive being gripped, resulting in more complex loading, a larger effective gage length, and errors in strain measurement. To correct this issue, a direct gripping method where poly methyl methacrylate (PMMA) blocks are used to clamp onto the fiber directly has been developed by Sanborn et al., and tensile tests have been performed at quasi-static (QS) strain rates with a novel single-fiber tensile testing device as well as at high strain rate (HSR) using a small-diameter tensile Hopkinson bar [11]. Important conclusions of this research involve UHMWPE displaying a high degree of strain rate dependence at a wide range of gage lengths. As seen in Figure 2.2, as strain rate increases, stiffness and strength generally increase, but failure strain decreases. This result is primarily due to increased linearity in stress-strain behavior as strain rate increases. Based on the data, the high-rate modulus ranges from 164 GPa to 136 GPa as gage length increases from 5 to 10 mm.

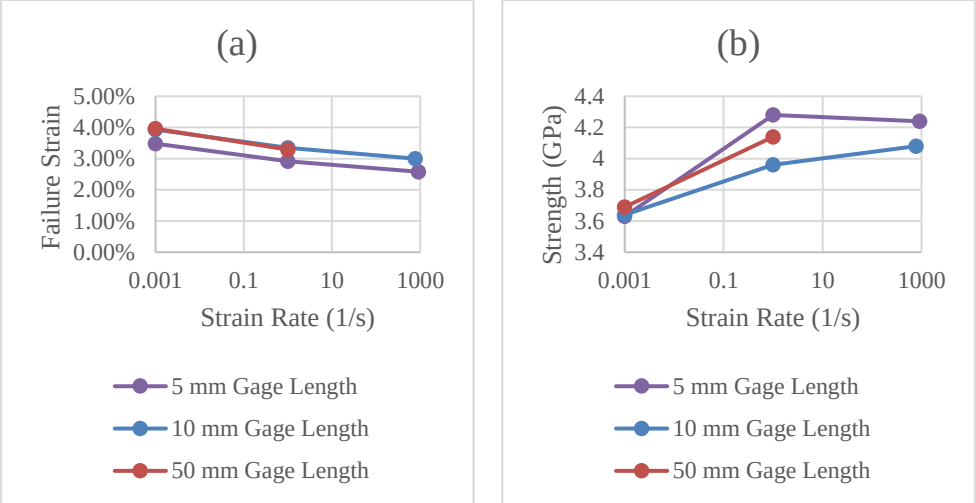

Figure 2.2 Effects of strain rate and gage length on (a) failure strain and (b) strength [11]

Russell et al. have performed an extensive study on failure of the Dyneema® SK76-reinforced polyurethane laminate material HB26 which incorporates primarily yarn characterization at varying strain rates with some single fiber work at low strain rates in order to verify the accuracy of methodology [12]. Slow-rate, laminate-level tension tests are coupled with microscopy and scanning electron micrographs to identify damage failure characteristics in various laminate designs as seen in Figure 2.3(a). Yarns are tested using the apparatus in Figure 2.3(b), where the yarn is wrapped around two pins and fastened to an anvil which is translated at varying rates to control the strain rate. Pins are connected to load cells for stress determination, and gage length is reported as effectively 5 mm for comparison to equivalent data and strain calculation. A significant reduction in strength is seen compared to single fiber strength values. This is explained as a combination of gripping methods inducing a strength reduction, which is corrected, and inherent fiber waviness in the yarn resulting in an apparent strength reduction. Strain rates of tests range from 10^{-4} to 10^{3} s^{-1}, and initial modulus is determined from stress-strain data. Some increase in stiffness is seen from QS to intermediate dynamic rates, but the modulus levels

off around 130 GPa as strain rates increase further toward 10^3. This reported stiffness value is relatively consistent with observations by Sanborn, albeit somewhat smaller considering the small gage length. This difference is most likely a combination of standard reductions due to fiber waviness in the yarn and some added reduction due to incongruity in testing methods.

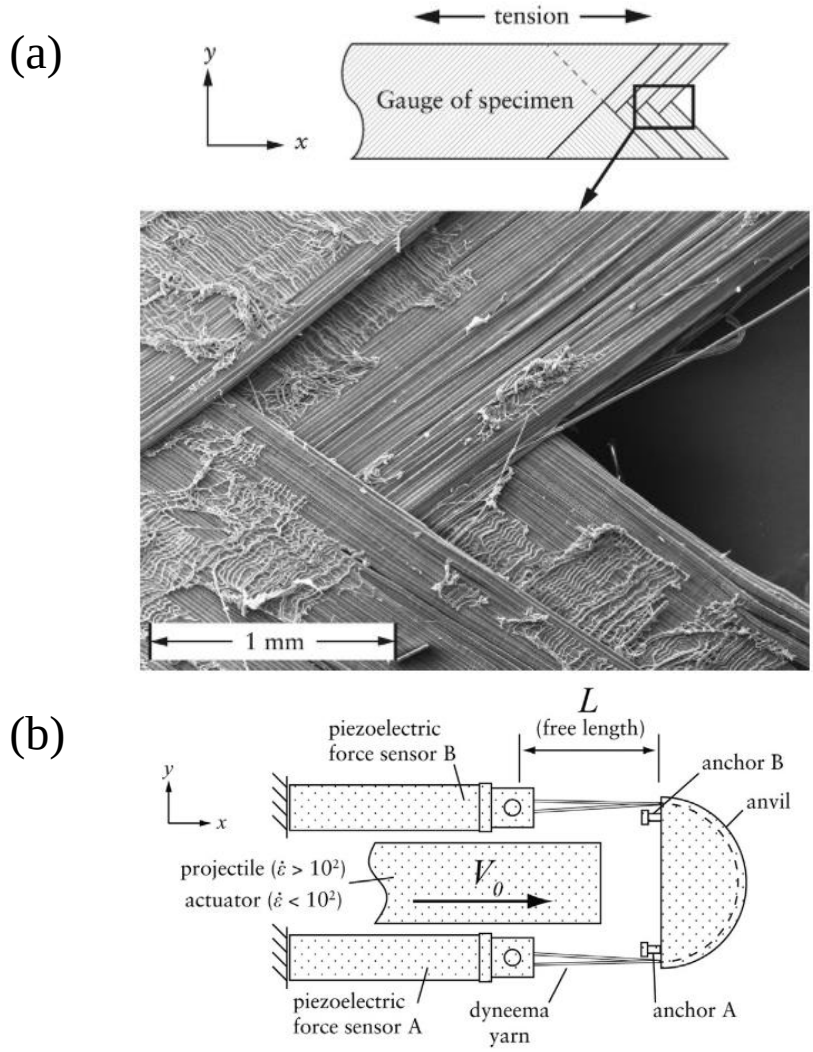

Figure 2.3 (a) Scanning electron micrograph of fracture site in ±45° UHMWPE laminate. (b) High-rate yarn testing apparatus

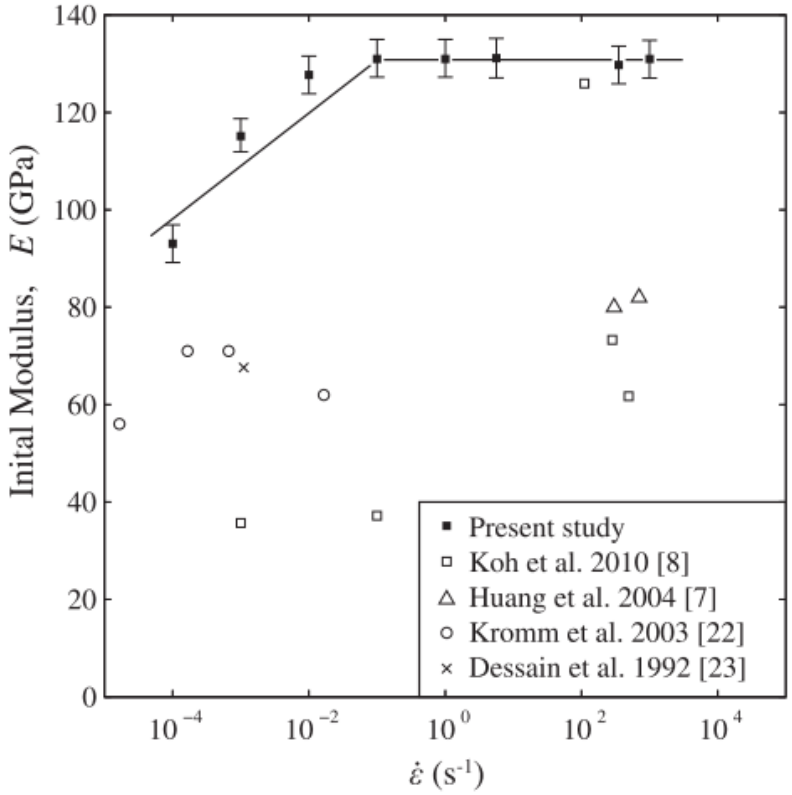

Figure 2.4 Initial modulus measurements for high-rate yarn loading in Russell et al. [12]

2.3 MULTIAXIAL LOADING OF SINGLE FIBERS

Transverse properties of single fibers are difficult to obtain through conventional means, so various novel methods for quantifying single fiber mechanical behavior have been developed. Cheng et al. have utilized a piezoelectric translator to transversely load Kevlar® KM2 single fiber and obtain a transverse elastic modulus [13].

Quantification and prediction of the behavior of a single fiber under transverse impact has been a focus of research efforts, but most progress on this front has been accomplished through finite element modeling, with results related to experiments performed with different loading conditions or lower strain rates. These models are sometimes done with Kevlar® KM2 as the target material, but the methods are generally

applicable to UHMWPE as well. Sockalingam et al. have produced a model for the compression of a single yarn tow within a woven laminate based on individual fiber deformation and expanded to modeling single fiber impact behavior, comparing results to existing analytical solutions[14], [15]. Furthermore, experimental data from single fiber transverse loading has been incorporated into a LS-DYNA user material subroutine (UMAT) to more effectively replicate inelastic behavior as a result of transverse loading [16]. This method has been applied to model the behavior of Kevlar® KM2 under multiaxial loading at QS strain rates as illustrated in Figure 2.5, and a failure criterion based on maximum strain has been developed to predict failure based on maximum strain as output by model data based on failure strain and strength modulation factors such as contact length (L_c), axial compression (AC), transverse compression (TC), transverse shear (TS), and strain rate (SR) which is described in Equation 2.4.

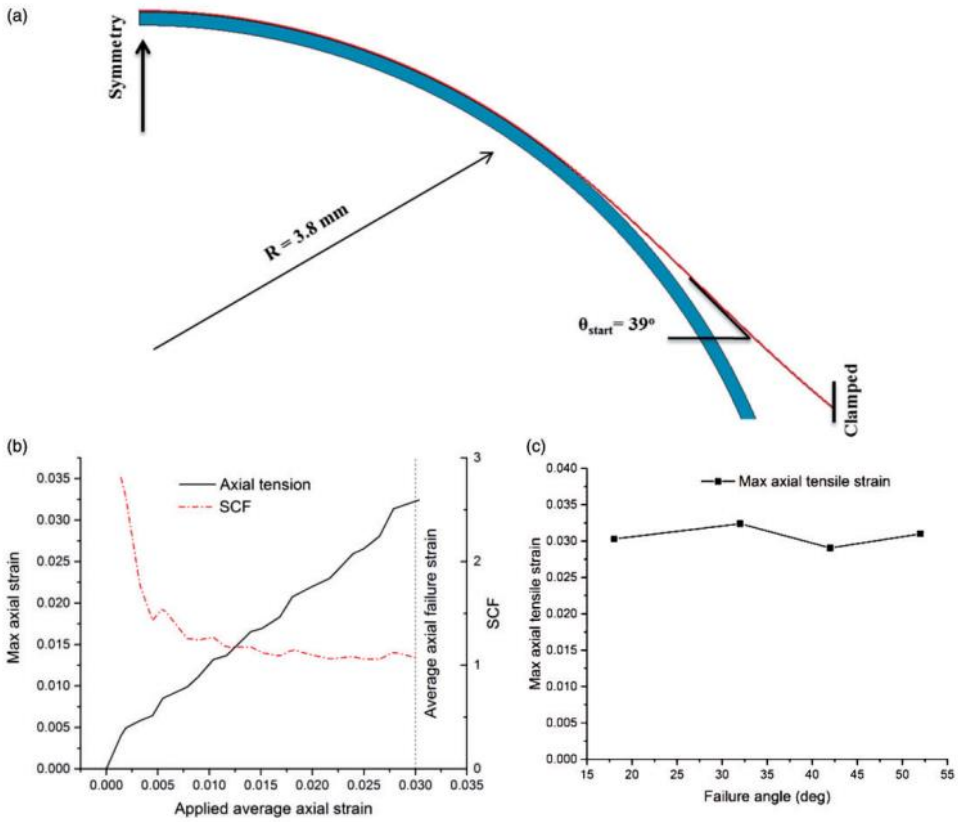

Figure 2.5 (a) Fiber model transversely loaded. (b) Maximum axial tensile strain evolution with stress concentration factor for 32° failure angle. (c) Comparison of failure strain as a function of failure angle.

$$\frac{\varepsilon_{3,\max}}{\varepsilon_{3,\text{fail}}} = 1 \tag{2.4}$$

Where:

$$\varepsilon_{3,\text{fail}} = \varepsilon_3(L_c, \text{ACr}, \text{TCr}, \text{TSr})$$

$$\varepsilon_{3,\text{fail}} = \varepsilon_3(L_c) \times (1 - \text{AC}) \times (1 - \text{TC}) \times (1 - \text{TS}) \times (1 + \text{SR})$$

For the failure criterion, $\varepsilon_3(L_c)$ is a gage length-dependent theoretical failure strain based on a Weibull distribution, which allows for predicting the probability of failure as a function of gage length and applied strain as in Equation 2.5. When solved for applied

strain, the 50% breaking strain (ε) is calculated based on gage length (L) and failure strain (ε_0) at a reference gage length (L_0) as in Equation 2.6 [17], [18].

$$P(\varepsilon, L) = 1 - exp\left[-\frac{L}{L_0}\left(\frac{\varepsilon}{\varepsilon_0}\right)^m\right] \tag{2.5}$$

$$\varepsilon = \varepsilon_0\left(-\frac{L_0}{L}\ln(0.5)\right)^{\frac{1}{m}} \tag{2.6}$$

Based on the data of Sanborn et al., for reference gage length of 10 mm and failure strain of 0.0405, the shape parameter (m) is equal to 13. The predicted failure strain as a function of gage length can be seen plotted with the expected bounds as well as the failure strain of a perfect polyethylene crystal chain (approximately 10%) in Figure 2.6 [19].

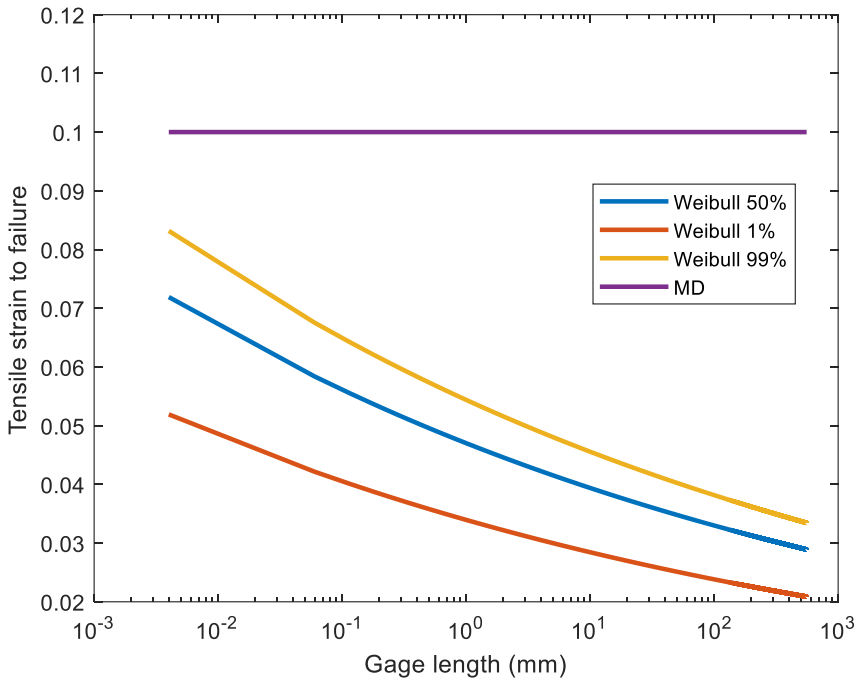

Figure 2.6 Gage length-dependent axial tensile failure strain for Dyneema® SK76 UHMWPE fiber

Experimental progress has been made toward identifying the effects of initial loading on the tensile strength and failure strain of UHMWPE. Hudspeth et al. have

developed a system for simultaneously applying torque and dynamic tension to single UHMWPE fibers, and the results have been used to form a failure surface quantifying tensile strength reduction as a function of transverse shear (TS) stress as depicted with the loading apparatus in Figure 2.7 [20].

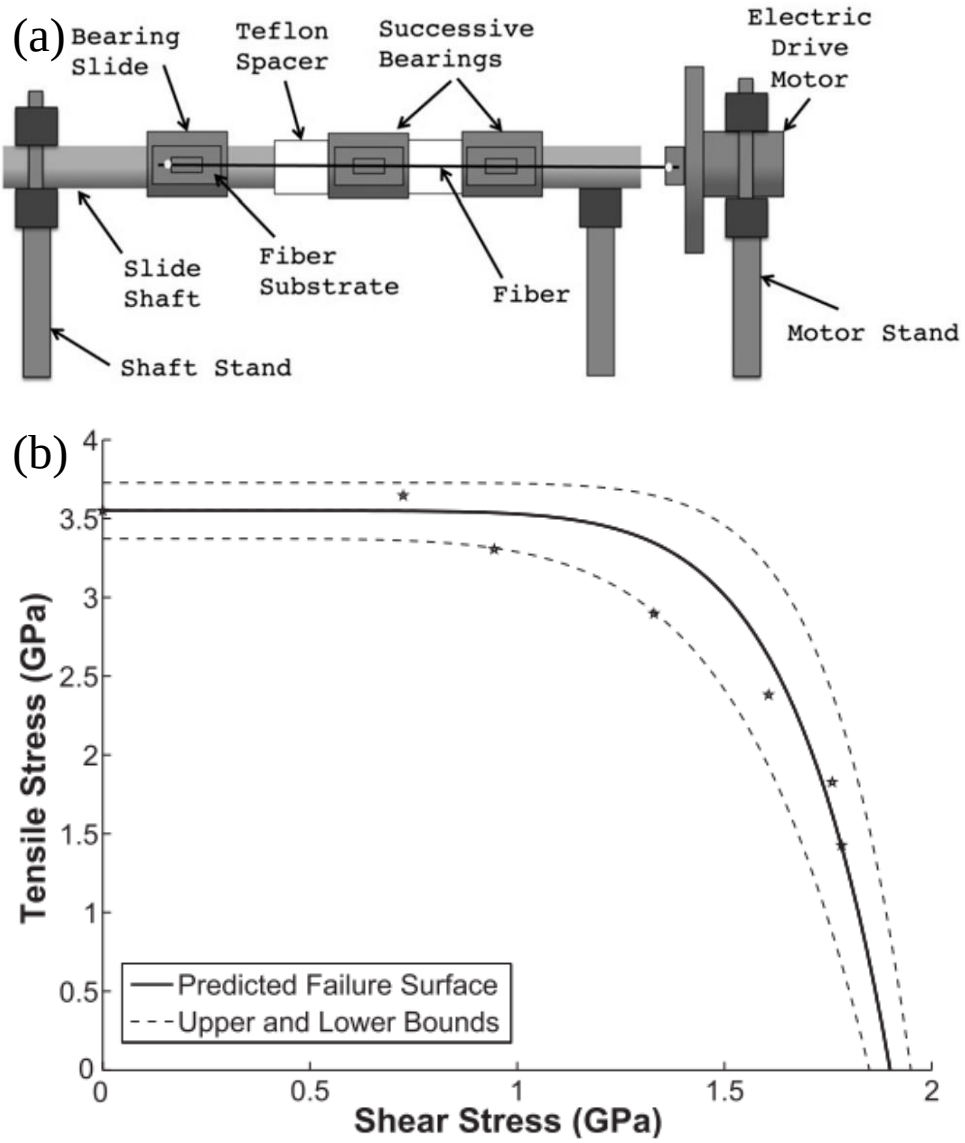

Figure 2.7 (a) Apparatus for applying torque to single fibers. (b) Biaxial shear/tension failure surface [20]

A study has also been performed by Hudspeth et al. examining the effects of geometry on yarn and single fiber failure strain under QS transverse loading. Several indenter shapes were chosen, including a large-radius (3.8 mm) round geometry, a precision-designed 0.30 caliber fragment-simulating projectile (FSP) geometry (20 μm radius), and a razor (2.3 μm radius), and various initial loading configurations were applied to quantify the change in failure strain due to geometric effects. Measurements have been taken to verify the loading radius, as seen in Figure 2.8. The loading geometries and a schematic of the experimental setup are depicted in Figure 2.9. The large radius loading geometry does not demonstrate any significant failure strain reduction over standard tensile results, but both the FSP and razor demonstrate failure strain decreases as loading radius decreases and initial angle increases [21]. Scanning electron micrographs were taken of representative failed fibers as seen in Figure 2.10. Fibrillation is clearly seen from the round and FSP samples, where fiber shearing appears to be the primary failure mode for the razor sample. Failure strain as a function of breaking angle (which is influenced by increasing the starting angle) is displayed in Figure 2.11. While the round geometry demonstrates very little difference from tensile loading at most failure angles, the FSP clearly shows degradation in failure strain as starting angle increases despite being indistinguishable from the round geometry at very low angles. Razor loading demonstrates significant degradation at low angles, but as breaking angles increase, failure strain does not show demonstrate a clear trend. One challenge associated with this study is that the razor is effectively loaded at a point, but the FSP has two points of contact, resulting in more complex loading conditions, and the sharpened edges are nonstandard, increasing the difficulty of

replication. Even so, this study provides a preliminary standard for testing fiber strength under transverse deflection.

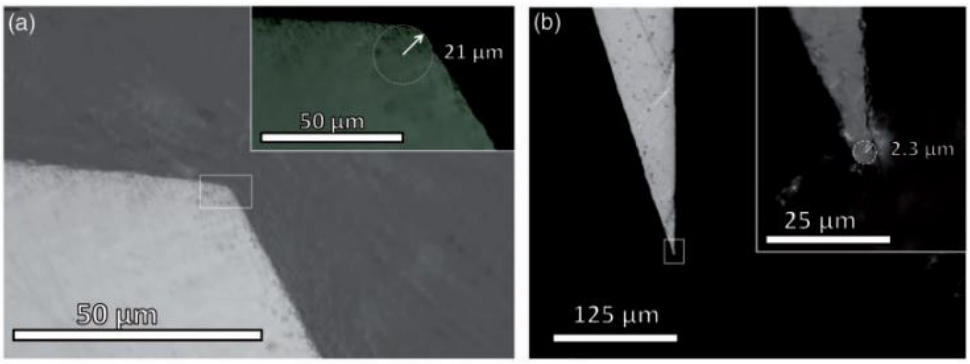

Figure 2.8 Radius of curvature measurements for (a) FSP and (b) razor cross-sections [21]

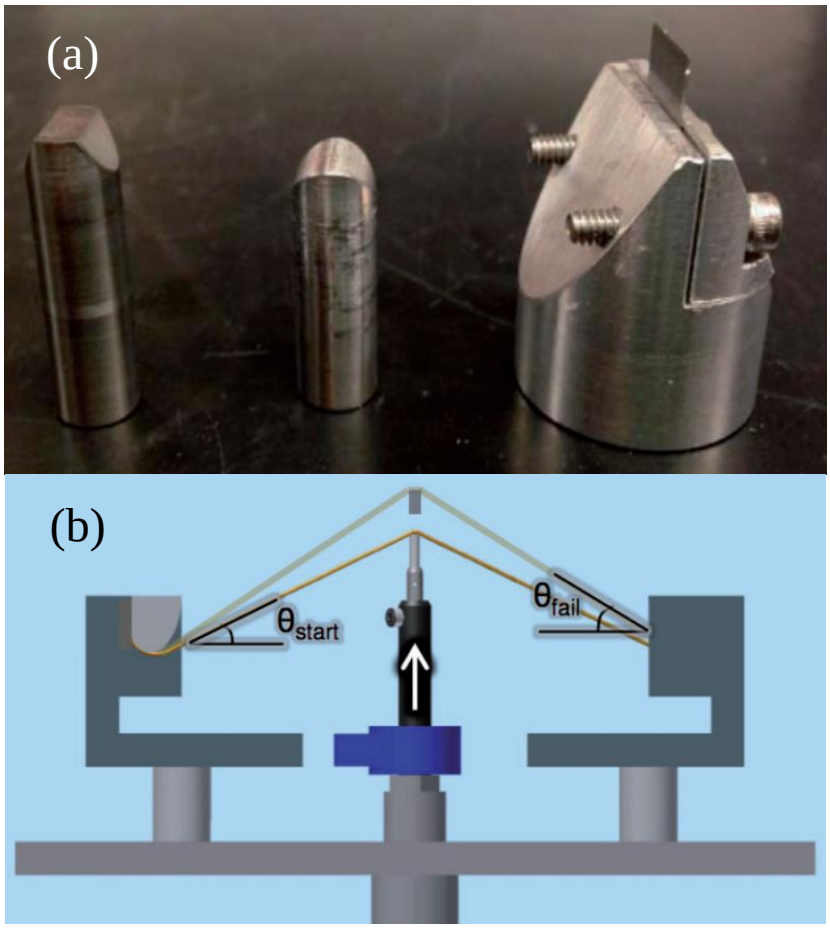

Figure 2.9 Experimental setup for QS transverse loading. (a) Indenter geometries from left to right: FSP, round, razor. (b) Test schematic for single fiber transverse loading [21]

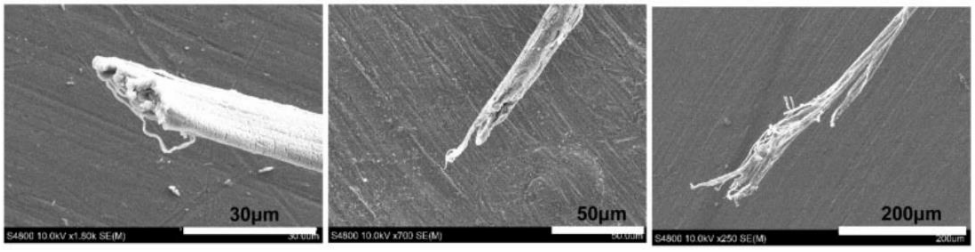

Figure 2.10 Scanning electron micrographs of fiber failure surface. From left to right: razor, FSP, round [21]

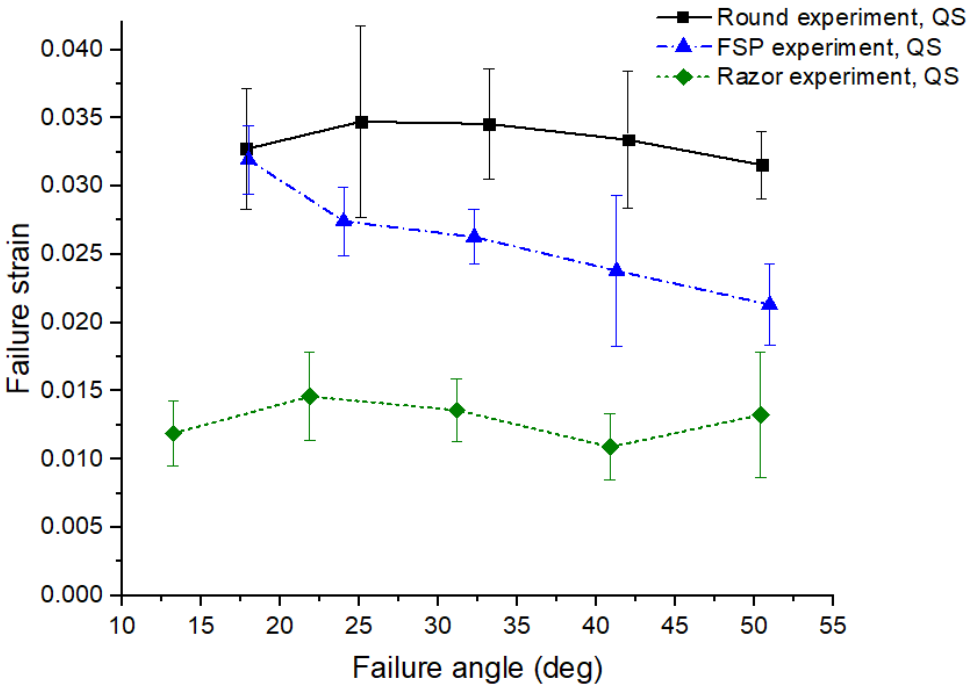

Figure 2.11 Failure strain correlated with angle of failure [21]

Some initial efforts have been made to investigate the effects of dynamic loading on UHMWPE fiber failure. Such a characterization would be essential to linking macroscopic behaviors to micro-scale studies such as the work of Stockdale et al. on UHMWPE fibrillation the work of Lee et al. on nanocomposite HSR deformation [1], [22].

2.4 SUMMARY

Transverse impact behavior of high-performance fibers is an important research objective for predicting the efficacy of ballistic armor systems. Initial work has been yarn-based with analytical models predicting response immediately after impact, with some emphasis on failure as a result of instantaneous rupture. Later work has moved to quantifying single-fiber tensile strength at various strain rates. Modeling work has been done for quantifying failure behavior of Kevlar® KM2 under transverse impact, with some experimental data inputs improving failure estimates.

For UHMWPE, testing has been performed to quantify the pure axial strength and failure strain as a function of strain rate and gage length. This data has then been used to create a Weibull model and provide a baseline for various experiments. Investigation has been made into the strength and failure strain reduction caused by multiaxial loading conditions such as constantly applied transverse shear in the form of torque as well as by inducing transverse deflection. HSR transverse compression is demonstrated to reduce tensile strength under QS conditions. This data has been incorporated into simulations which are used to identify stress concentrations and drive failure criterion development. However, further efforts are required to quantify the performance of these fibers under HSR conditions.

CHAPTER 3

INFLUENCE OF HIGH STRAIN RATE TRANSVERSE COMPRESSION ON THE TENSILE STRENGTH OF UHMWPE SINGLE FIBERS

This chapter presents a method for characterizing the residual tensile strength of single UHMWPE fibers under both QS and HSR conditions. Fibers are compressed by a small-diameter Kolsky bar at high nominal strain rates and tested in tension for stress-strain behavior. The strength reduction factor is then used to correlate model results to experimental failure data for transverse loading.

3.1 METHODS

The HSR experimental set up involves compressing a single fiber in a smaller diameter Kolsky bar set up as shown in the schematic in Figure 3.1. The steel incident and transmitted bar diameters are 3.175 mm and 0.283 mm respectively. A semiconductor strain gage on the incident bar is used to record the input pulse. Optical instrumentation using a normal displacement interferometer (NDI) is used at the free end of the transmitted bar to record the particle velocity [23]. The compressive load per unit length (F) and displacement (u) of the fiber are measured in real time. Compressed width (2w) and original fiber diameter (2r) are measured post-test. The fibers are compressed at nominal strain rates (velocity divided by original fiber diameter) in the range of 10,000 to 90,000 1/s and the corresponding particles velocities are in the range of 0.20 to 1.10 m/s. The applied strain rate is varied by controlling the pressure applied to accelerate the striker bar.

However, in this set up it is difficult to control the applied maximum nominal strain at a given strain rate. A more detailed explanation of the experimental set up is given in [23].

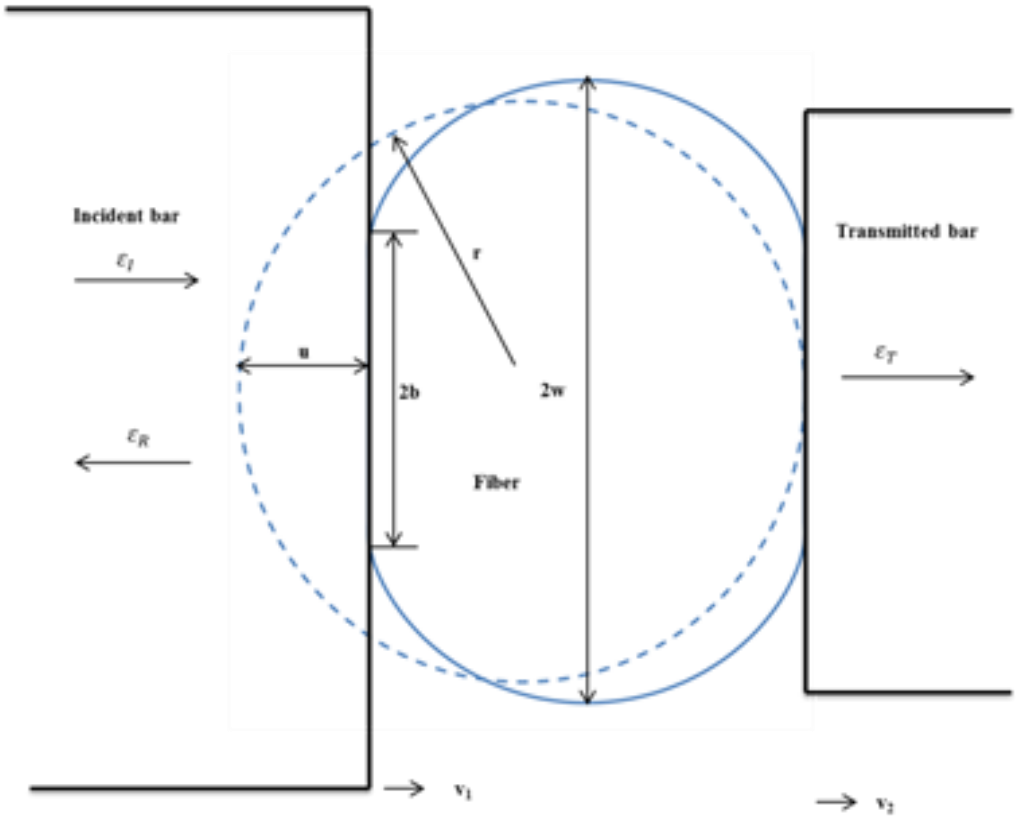

Figure 3.1 Schematic of single fiber HSR transverse compression (not to scale)

For QS tensile loading, a Psylotech nTs single-fiber testing apparatus is used, and for HSR loading a custom high-rate Hopkinson tension bar is used. Both utilize a direct gripping method between polycarbonate blocks as described in [11], where individual fibers begin in a window frame fixture for ease of loading, and the sides of the frame are removed once the clamps are in place and testing is ready to begin. Figure 3.2 is a representative fiber window frame sample.

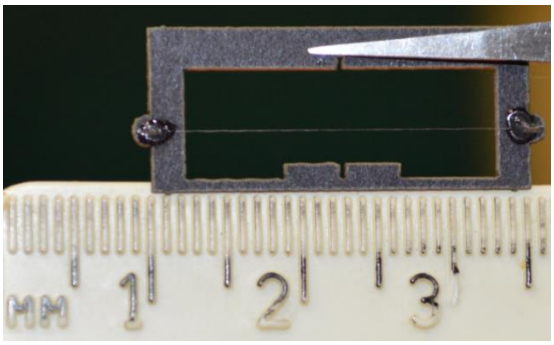

Figure 3.2 Single fiber window frame

35 samples are transversely loaded and then placed into one of two groups: 17 samples are tested under QS conditions, and 18 are tested under HSR conditions. Figure 3.3 contains schematics of each experimental setup.

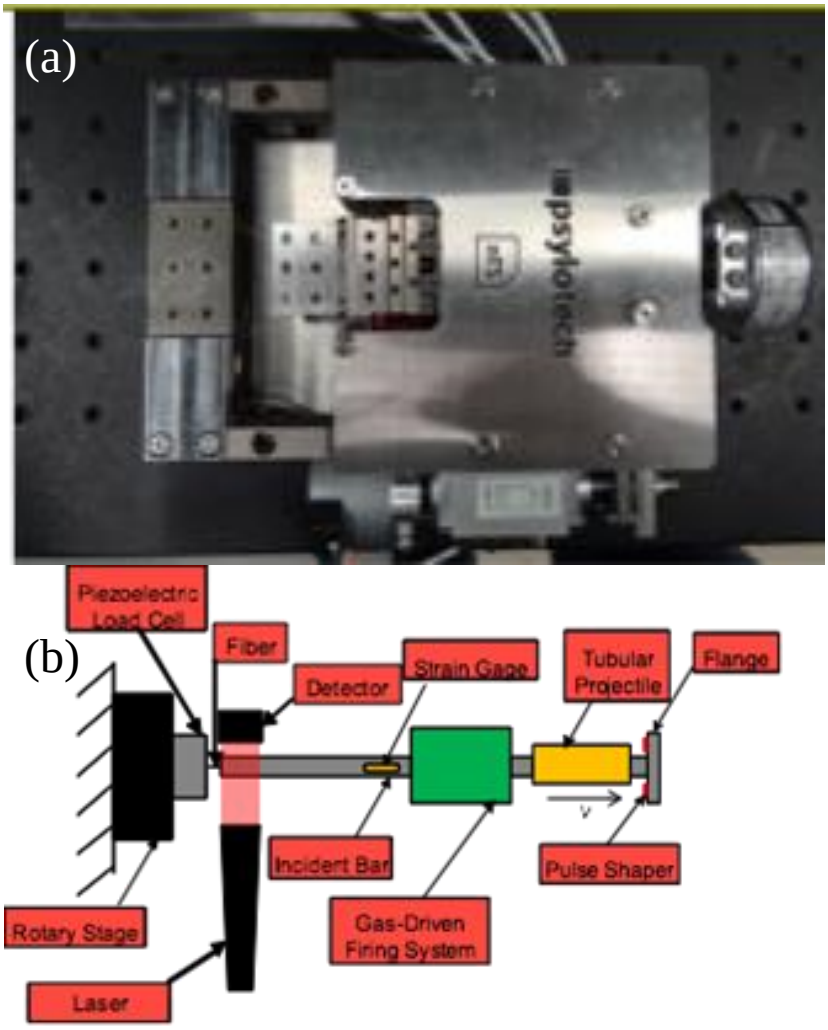

Figure 3.3 Schematics of single fiber tensile apparatus. (a) Psylotech nTs for QS tests. (b) Hopkinson bar for HSR tests.

3.2 RESULTS AND DISCUSSION

Samples are transversely compressed, and stress strain diagrams are compiled in Figure 3.4.

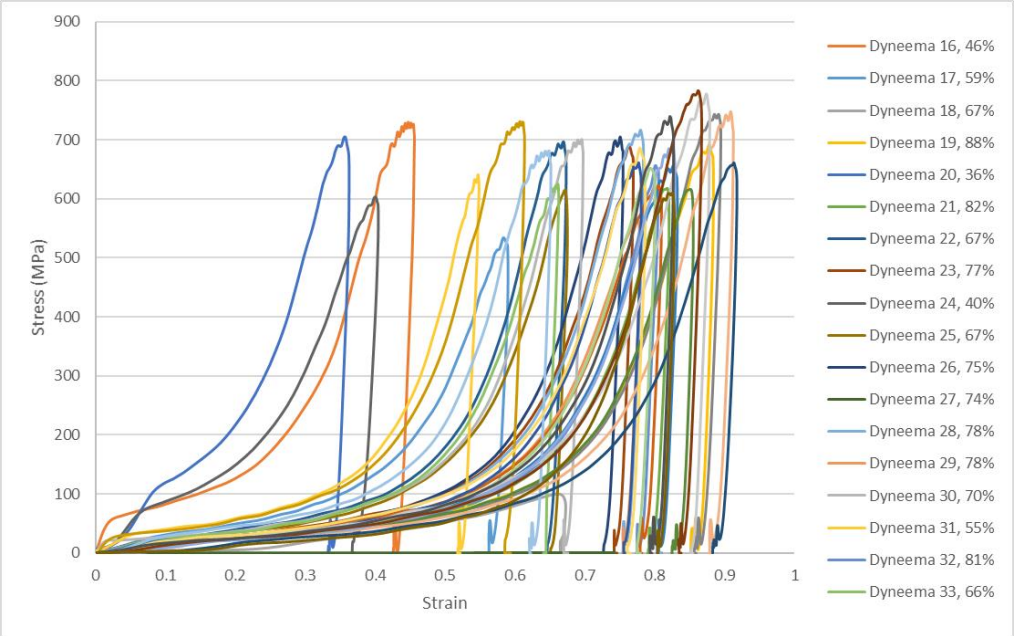

Figure 3.4 Nominal stress strain behavior in compressive loading of Dyneema SK76.

After transverse loading but prior to tensile testing, all samples are measured under confocal microscopy for deformed region width (2w) and undeformed fiber diameter (2r). Figure 4 shows a confocal microscopy image of a damaged Dyneema® SK76 fiber. It is seen that the fiber is compressed uniformly along the length of the compressed region. Contact width (2b) is not easily determined from the scanned images.

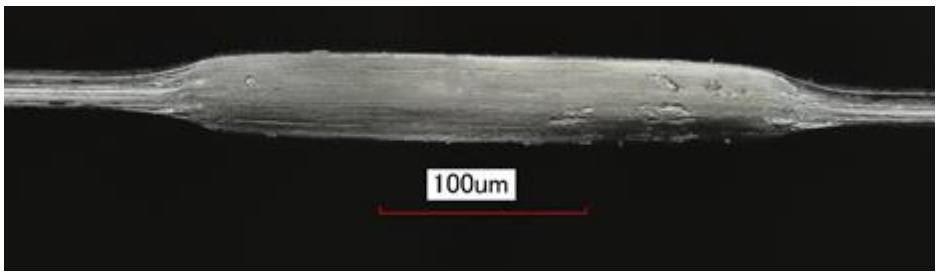

Figure 3.5 Confocal microscopy image of Dyneema SK76 at 54,117 1/s to 70% nominal strain.

Normalized effective contact width has previously been defined as $2w_{eff} = \frac{2w+2b}{2}$ [9], but because 2b is impossible to reliably measure, 2w is assumed to be a reasonable estimate of $2w_{eff}$. Failure is expected in the compressed region, so the stress calculation

had originally been planned to be defined as $\sigma = \frac{F}{2w \times (2r-u)}$. However, a high degree of variation is present in the measured values, which results in a large variance in calculated stress even though a much lower variance is observed in the measured breaking force. Thus, the undeformed fiber cross-sectional area based on 2r is used, as this yields much more consistent values. The decision to use this method is further supported by the fact that failure is not always observed within the compressed region. Even in tests where this may possibly be the case, confirmation is difficult because fibrillation that occurs as a result of testing render the compressed region unrecognizable. The experimental nominal stress ($\bar{\sigma}$) is defined by Equation 3.1, where *F* is the breaking force and *A* is the undeformed fiber area.

$$\bar{\sigma} = \frac{F}{A} \tag{3.1}$$

Nominal strain ($\bar{\varepsilon}$) is defined by Equation 3.2, where *u* is the displacement, and *l* is the gage length between the grips.

$$\bar{\varepsilon} = \frac{u}{l} \tag{3.2}$$

Nominal stress-strain plots of representative samples are included in Figure 3.6. Some samples could not be plotted due to slippage distorting strain calculations, but the tests represented below were all successful.

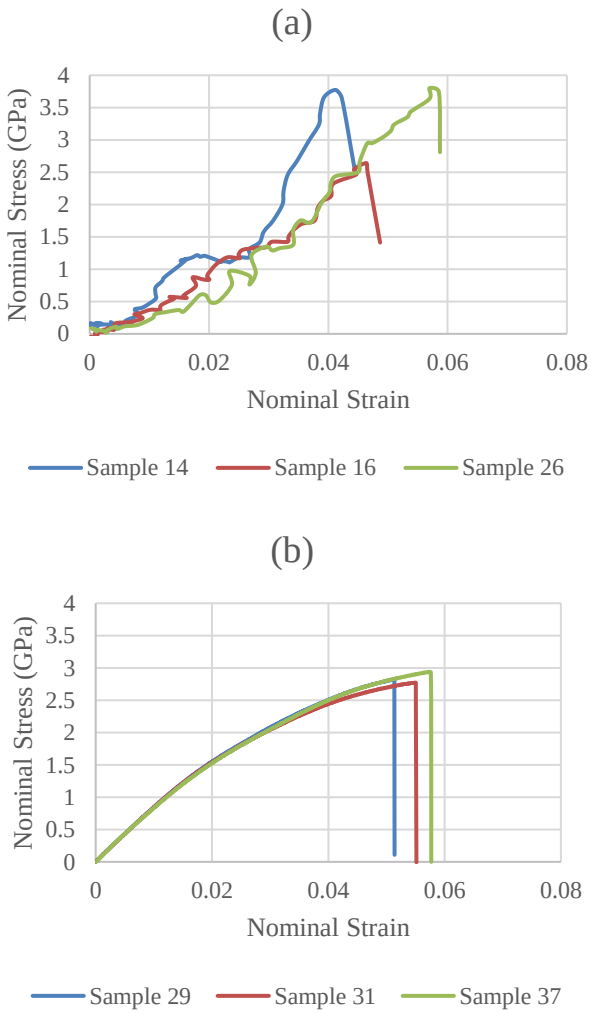

Figure 3.6 Nominal stress-strain of representative samples. (a) HSR (~1000 1/s strain rate). (b) QS (0.001 1/s strain rate). Nominal area is original fiber area, and nominal gauge length is 10mm.

Average maximum stress in QS and HSR tests are compared to strength values of uncompressed Dyneema SK76 fibers at identical gage lengths and similar strain rates as determined in [11]. Figure 3.7 compares mean strength between groups with 95% confidence intervals based on standard deviations. Confidence intervals between compressed and uncompressed groups at similar strain rates do not overlap, indicating a significant decrease in strength due to the compression. ANOVA with post-hoc Tukey test

provide confirmation that decreases in strength, approximately 19.6±3.6% for QS and 13.2±9.5% for HSR, are significant with α=0.05.

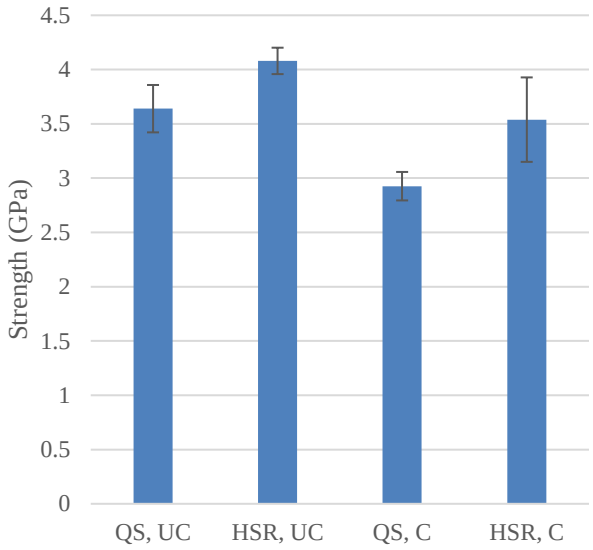

Figure 3.7 Mean maximum stress with 95% confidence intervals. Uncompressed (UC) sample values based on [11]. Compressed (C) sample values from experimental data.

Maximum tensile strength of each fiber is also graphed on a Weibull probability plot to obtain the Weibull strength parameters. Figure 3.8 represents the HSR and QS probability plots, with the uncompressed strength data included for reference in each case. Table 3.1 presents Weibull parameters as a function of strain rate in comparison with parameters for uncompressed fibers, based on data from [11]. For both experiments, the characteristic strength is reduced as expected. However, for the QS experiments, Weibull modulus, an indicator of strength variability, is largely unchanged, unlike the HSR experiments which demonstrate a much lower modulus due to the wider data spread.

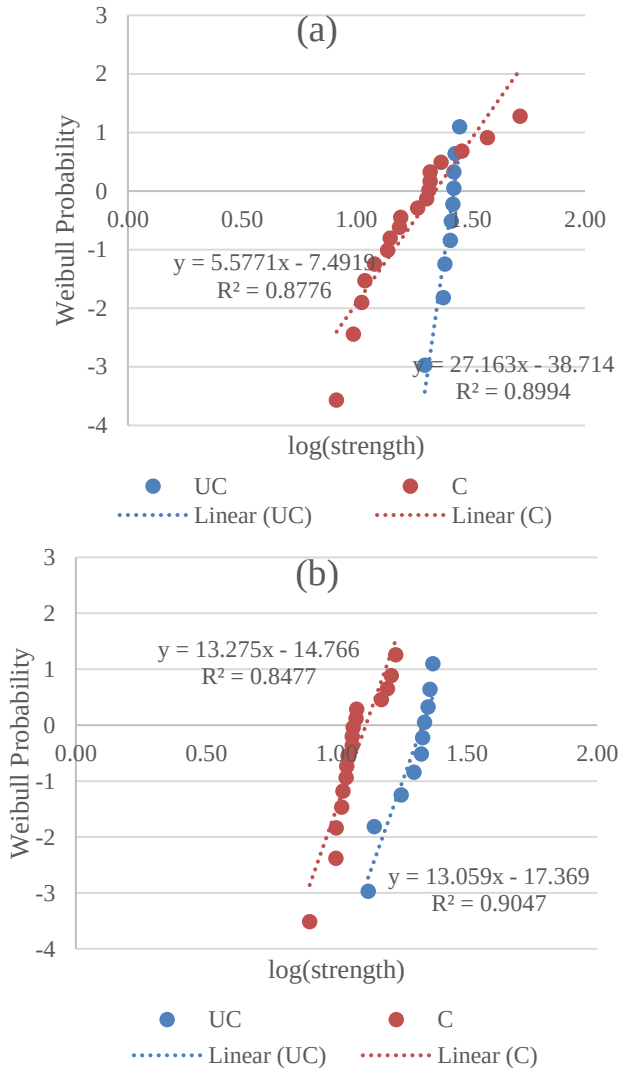

Figure 3.8 Weibull probability plots for uncompressed (UC) and compressed (C) fibers for each strain rate. (a) HSR (~1000 1/s strain rate). (b) QS (0.001 1/s strain rate)..

Table 3.1 Weibull parameters based on strain rate and damage

	Uncompressed Fibers		Compressed Fibers	
Rate	**Weibull Modulus (β)**	**Characteristic Strength (GPa)**	**Weibull Modulus (β)**	**Characteristic Strength (GPa)**
QS	13.059	3.781	13.275	3.041
HSR	27.163	4.159	5.577	3.832

3.3 SUMMARY

This chapter presents a novel method for quantification of single-fiber strength degradation due to transverse compressive loading. Individual fibers are transversely loaded via small-diameter Kolsky bar and tested for residual tensile strength under QS and HSR conditions. Damage is visible under microscope imaging, and strength reduction is 19.6% for QS and 13.2% for HSR. These results demonstrate the measurable effects of transverse loading on tensile strength, which is necessary for identifying its contribution to failure under high-rate multiaxial loading.

CHAPTER 4

EXPERIMENTAL DESIGN FOR SINGLE FIBER TRANSVERSE IMPACT

This chapter presents a novel method for testing single fibers under dynamic multiaxial loading. A small-diameter Hopkinson compression bar is modified to launch specified impacting geometry at a controlled rate. Test progression is recorded via load cells and high-speed camera, which are used to calculate nominal stress, impact velocity, and average strain. Results are compared to

4.1 METHODS

4.1.1 Transverse Impact Apparatus

For slow to intermediate rate loading conditions, universal testing machines have been repurposed for applying transverse loading as in Hudspeth et al. [21]. However, HSR dynamic loading is often accomplished using various types of Hopkinson bar. In a standard Hopkinson compression bar (Kolsky bar), a pressure vessel launches a striker bar into contact with an incident bar with a wave shaper at the point of contact, which results in a strain pulse being sent through the bar at the material's internal wave speed. The traveling strain wave results in discrete motion in the bar, which is in contact with the material being tested. When the strain wave reaches the end of the bar, part of the wave is reflected back into the bar, and part is transmitted through the material, which is then transmitted to another bar (transmission bar) on the opposite side of the material. Strain gauges on both

the incident and transmission bar are used to determine the material response under the induced dynamic loading conditions. Such a method was applied to induce transverse compression damage in Thomas et al. [24], and the ability to induce loading in a controlled fashion is advantageous, but the standard configuration is insufficient for controlling the loading geometry and observing fiber failure.

To perform testing, a 0.25” diameter Al 7075 Hopkinson compression bar with a 6’ long incident bar and 24” long striker bar is modified to allow for single fiber transverse loading. A schematic of the final apparatus is shown in Figure 4.1. Several changes have been made to the setup for the purpose of this testing method. First, the transmission bar is removed as it serves no purpose. Next, a U frame is mounted such that the fiber can be gripped transversely to the motion of the incident bar. Fibers are held in place using the direct gripping method utilized in Sanborn et al. [11], where fibers are glued to cardboard window frames for easy handling before being placed in the grips, where the fiber is clamped between PMMA blocks and the frame is cut to so as to not impede testing. 50 mm frames were used, which result in a 41.6 mm gage length when the fiber is finally loaded. Finally, a fixture for holding the indenting geometry must be produced, as impacting the fiber with the bar alone would be difficult to capture on camera and result in complex loading conditions. Additionally, the motion of the incident bar is limited to discrete periods of acceleration due to its considerable length, which also results in inconsistent loading over time. To mitigate these problems, a 1.5” nylon sleeve with a 0.45” minimum outer diameter as depicted in Figure 4.2 is placed over the end of the bar. A hole with just under 1 mm diameter is drilled 0.2” deep on one end to allow for compression fitting of

indenter geometries, and the other end is bored out 1” deep with a 0.25” diameter to enable a tight but mobile fit over the end of the incident bar.

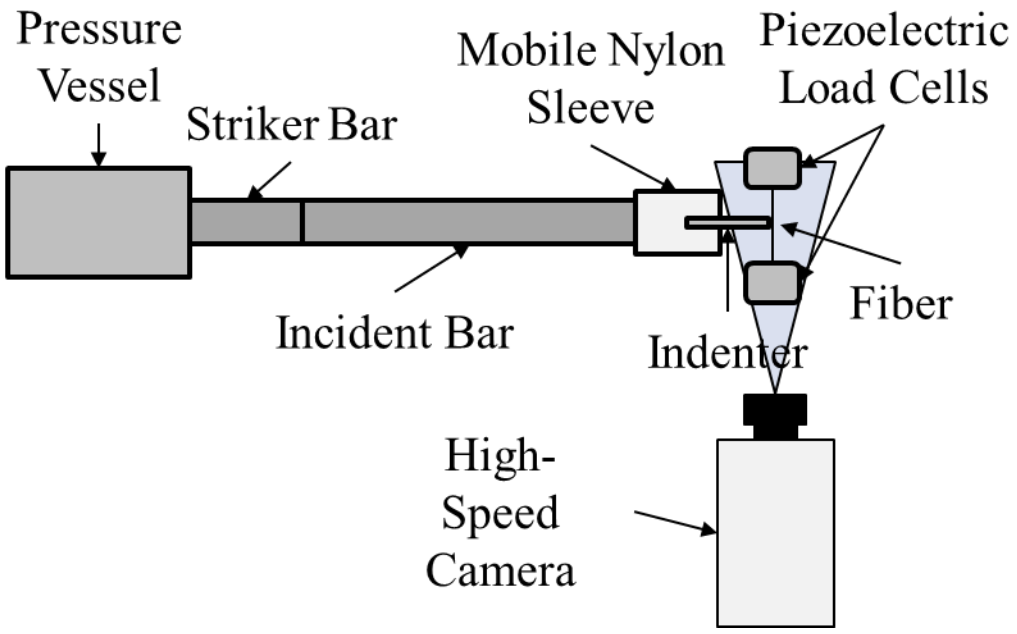

Figure 4.1 Schematic and image of experimental apparatus for single fiber transverse impact

Figure 4.2 Nylon sleeve with indenter

In the resulting configuration, a small amount of laboratory grease is placed on the end of the incident bar to serve as a wave shaper, the fiber sample is mounted in place and aligned with the indenter tip without inducing preload, the pressure vessel is filled to a specified level, and the pressure is released to launch the striker bar. When the stress pulse

is transmitted to the end of the incident bar, the sleeve and indenter are launched into the fiber, and the experiment is recorded for analysis.

4.1.2 Data Collection Methodology

Due to the novel nature of this experiment, data collection and analysis is a challenge. Strain gages are normally used for load determination as well as impact velocity approximation with Hopkinson bars, but the mobile sleeve launching mechanism results in this data being less meaningful for determining the conditions experienced by the fiber. For slower rate tests, load cells can be placed under the indenter, but due to the necessary mobility of the indenter combined with the contribution of momentum effects to the fiber loading, measurements can only be taken at the grips. To this end, the fiber grips are mounted in piezoelectric load cells (Kistler 9712B5) which have a sampling frequency of 2 MHz and record 5 ms of data.

To supplement information obtained through load measurement, experiments are recorded on a Photron Fastcam SA-5 with a Nikon macro lens at 320x192 resolution at 100000 frames per second. Experiments are illuminated by low-heat LEDs to provide sufficient light but reduce thermal effects on the fiber and measurement components. Data recording is triggered by load signal threshold, and sufficient data prior to triggering is recorded for analysis purposes. The camera is aligned such that the center of the fiber is in frame from the beginning of the experiment until failure occurs, and all motion is in the focal plane of the lens. The shaft of the indenter has a known diameter and used to correlate image measurements such as displacement of a reference point between frames for the purpose of determining average velocity over the test progression. Additional measurements, such as fiber diameter measurements which are taken at the intended impact

location for use in stress calculations, are made via analysis of images obtained from a calibrated confocal microscope.

4.1.3 Indenter Design, Production, and Use

As a primary goal of this research is to ascertain the effects of loading geometry on the transverse impact performance of single fibers, selection of loading geometry is an integral component. Steel stock pins with 1 mm diameter are used as the base material for use with the nylon sleeve system. Due to the small diameter of the fiber, imaging of the failure location over the course of the entire test at the desired framerate requires smaller indenter geometry compared to geometries used by Hudspeth, but the overall scheme is retained in simplified form. All loading geometries, which can be compared in Figure 4.3, are circular at the point of contact with changing radius of curvature.

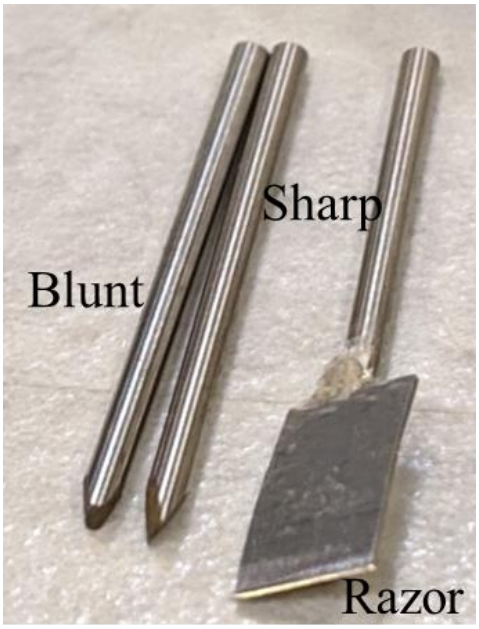

Figure 4.3 Comparison of indenter geometries

Razor blades (~2.0 μm radius) are still used, as the average radius is small enough to be captured by the system, and they provide an excellent baseline in terms of shear performance. Razor blade segments are isolated from fresh blades, which are broken apart

without damage to the edge, and secured to unused pins by cyanoacrylate glue, as a standard clamping system would add unnecessary bulk. The sharp impactor is designed to have a 20 μm radius similar to the FSP from Hudspeth, which is on the order of the fiber diameter, and the semicircular profile avoids the uncertainty regarding loading conditions that is present in the FSP geometry. The closest analogue to the 3.8 mm round geometry is the blunt indenter, which has a 200 μm radius. This radius is selected because it is an order of magnitude higher than both the fiber diameter and the sharp indenter. The expectation is that the blunt geometry has a large enough radius to induce failure largely due to tension. Both the blunt and sharp indenters are produced through electrical discharge machining, which offers the ability to produce small parts with a high degree of precision. Indenters are examined after production to verify that tip radius is reasonably close to nominal radius as depicted in Figure 4.4.

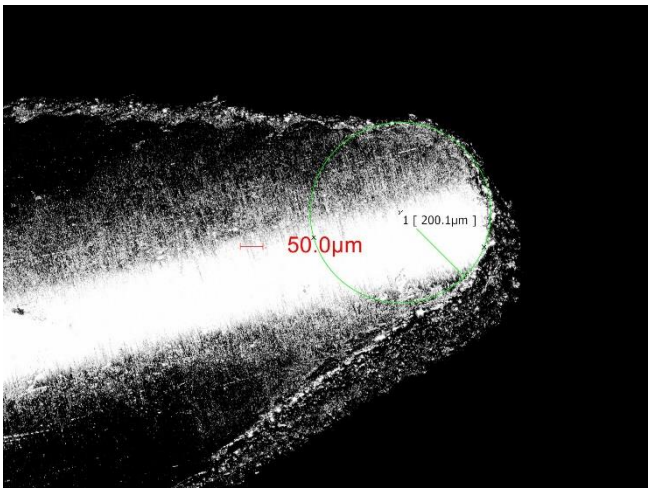

Figure 4.4 Microscope image of blunt indenter tip

Due to the high cost and difficulty associated with producing precise geometry via electron discharge machining, indenter reuse is necessary. While yarn-level experiments are expected to wear down an indenter over time, single fibers should not produce significant wear, especially on the blunt tip. Sharp indenters have been examined after

rounds of testing to verify the consistency of the tip, and the failure of the UHMWPE fiber does not appear to wear down the steel on any meaningful time scale. The primary exception is the razor projectile, which should be used no more than twice because the sharpness is its primary feature, and the brittle glue securing the blade segment to the pin can break, even after one test, so a mid-test failure would lead to a wasted specimen and unnecessary frustration. As a common laboratory implement, the razors can be obtained easily at little expense, and the pin to which the razor segments are glued can be reused if the glue breaks off, as it is prone to do.

4.2 RESULTS AND DISCUSSION

Data is obtained from the testing apparatus in two forms: load cell recordings at both fiber endings and test progression imaging. Representative load cell data is visible in Figure 4.5, and representative images used in analysis are displayed in Figure 4.6. This data is then post-processed to determine important quantities such as average impact velocity, average strength, average strain, and angle at failure. Tests are excluded based if failure does not appear to occur under the indenter based on the image data. Additionally, impact velocity generally correlates well to input pressure, but if a test has a substantially lower velocity for no apparent reason, it is excluded, as the intended strain rate levels are not achieved.

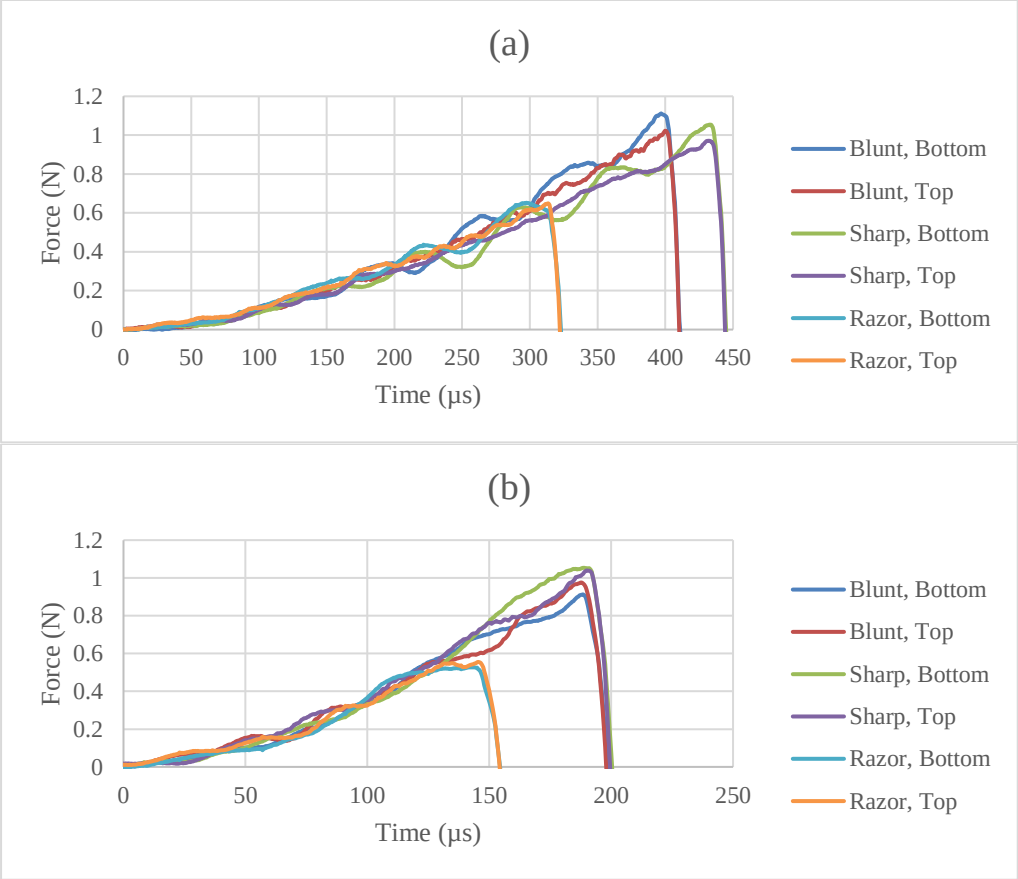

Figure 4.5 Representative load cell traces for (a) 10 m/s impact velocity (4295-4380 s^{-1} approximate strain rate) and (b) 20 m/s impact velocity (6805-6968 s^{-1} approximate strain rate)

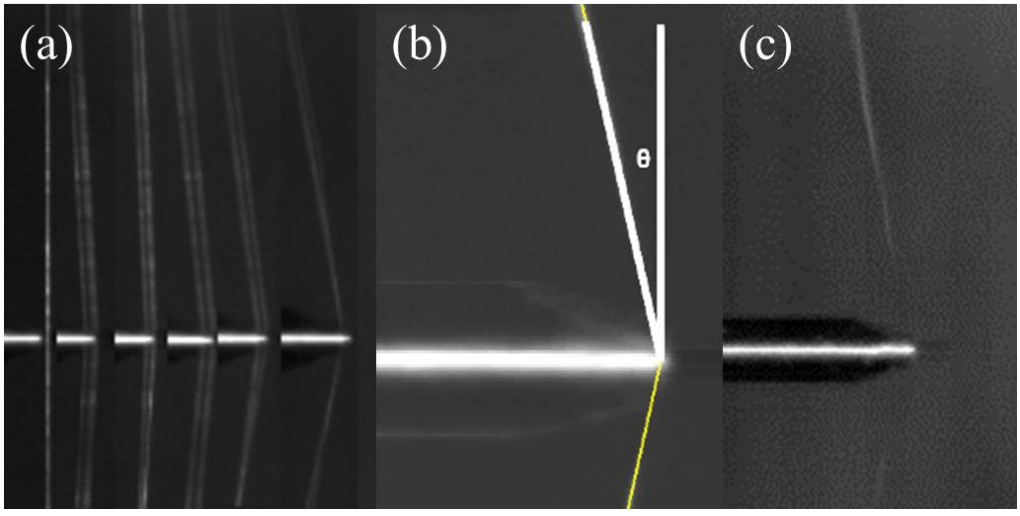

Figure 4.6 Experimental image analysis. (a) Progressive loading of single fiber. Images range from undeformed state (far left) to final ultimate tensile strain before failure (far right). (b) Angle measurement in final frame before failure. (c) Fiber motion post-failure.

4.2.1 Velocity Measurements

Two test speeds are selected to investigate the effects of strain rate variation on transverse strength. The independent variable in the experimental apparatus is pressure, where 5 psi is used to induce slow loading, and 15 psi is used to induce fast loading. Higher pressure levels risk damage to the existing setup, so for higher strain rates, the Hopkinson bar should be rebuilt to make it more robust. For each test, the displacement of a reference point in the focal plane between the initial loading frame and final loading frame is measured from an image such as (a) in Figure 4.6 via ImageJ, with the indenter diameter in each test used as a reference for 1 mm to yield a scale factor (SF). The displacement, measured in terms of the x coordinates of two reference points (p_0 and p_1), is converted to is divided by the elapsed time between measurement frames (Δt_v) to yield the average velocity (V) as demonstrated in Equation 4.1. Average velocities for each group are given in Figure 4.7.

$$V = \frac{SF(p_1 - p_0)}{\Delta t_v} \tag{4.1}$$

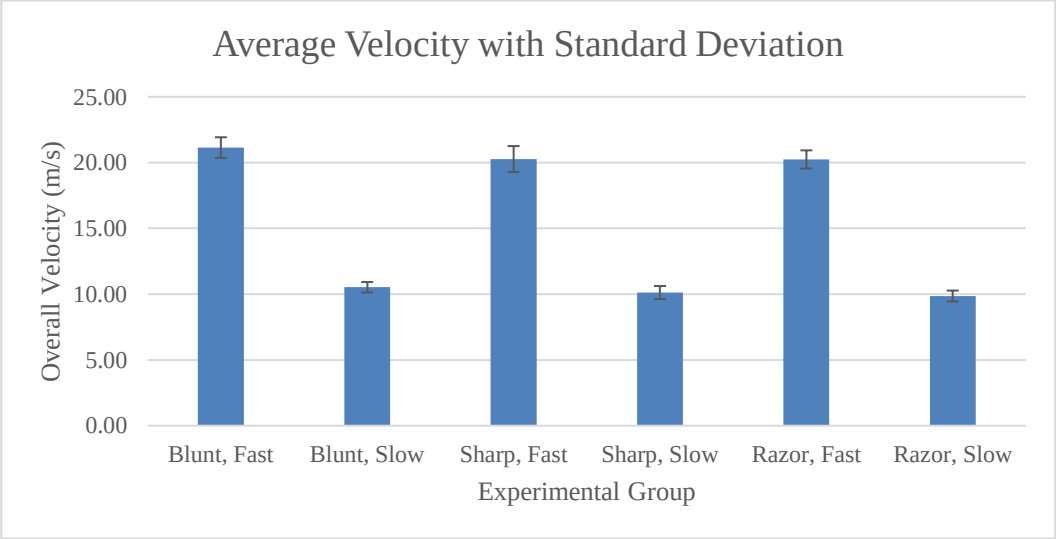

Figure 4.7 Experimental velocity comparison

Velocities are fairly consistent as a function of input pressure. A pressure setpoint of 15 psi correlates to approximately 20 m/s impact velocity, and 5 psi correlates to approximately 10 m/s. Blunt tests are slightly higher, but this is not expected to add significant strain rate effects compared to other geometries. Standard deviations are small, which indicates that tests within a group are comparable. Tests which have impact velocities which are outliers are excluded, as these induce strain rates outside the acceptable range for a given group.

4.2.2 Strength and Failure Strain Analysis

Strength, which is calculated according to Equation 4.2, is obtained from average maximum force in the load cell data (F_{avg}) and average measured fiber diameter (D_{avg}). Based on the assumption that maximum loads observed by the load cells represents the maximum load held by the fiber, strength can be calculated based on the initial area, which is obtained from diameter measurements prior to testing. Values are compared to tensile results from Sanborn et al. in Figure 4.8.

$$\sigma = \frac{F_{avg}}{\frac{1}{4}\pi D_{avg}^2} \tag{4.2}$$

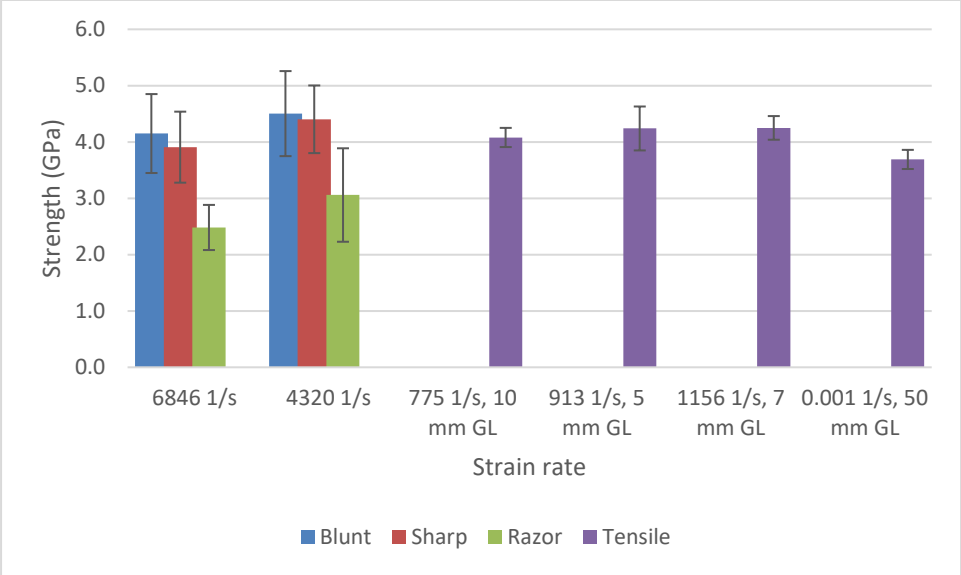

Figure 4.8 Average strength comparison with standard deviation

For both strain rates, strength is observed to be close to tensile results in the case of both blunt and sharp indenters, where the razor is considerably lower (40.18% reduced relative to blunt at high rate and 32.09% reduced at low rate). Controlling for geometry, the slower strain rate demonstrates a mild improvement in strength, where the blunt has an 8.53% increase, the sharp has a 12.66% increase, and the razor has a 10.39% increase. Sharp indenters appear to have slightly reduced strength compared to blunt, with a 5.82% reduction at high rate and 2.24% reduction at low rate.

Given the small scale and transient nature of the experimentation, strain is more difficult to quantify, as indirect means of measurement are required. Assuming the fiber is perfectly straight at failure, the displacement of the center of the fiber under the indenter (found by multiplying the velocity by the time to failure from the load cell data, Δt_f) can be used to calculate average strain through a simple Pythagorean relationship with gage length L_0 as demonstrated in Equation 4.3. In reality, some kinking of the fiber most likely exists, resulting in strain concentrations. However, this method is effective at quantifying

the average strain, which has been plotted in comparison to results from Sanborn et al. in Figure 4.9. Experimental data is also summarized in Table 4.1.

$$\varepsilon = \frac{\sqrt{\left(V \times \Delta t_f\right)^2 + (0.5L_0)^2}}{0.5L_0} - 1 \tag{4.3}$$

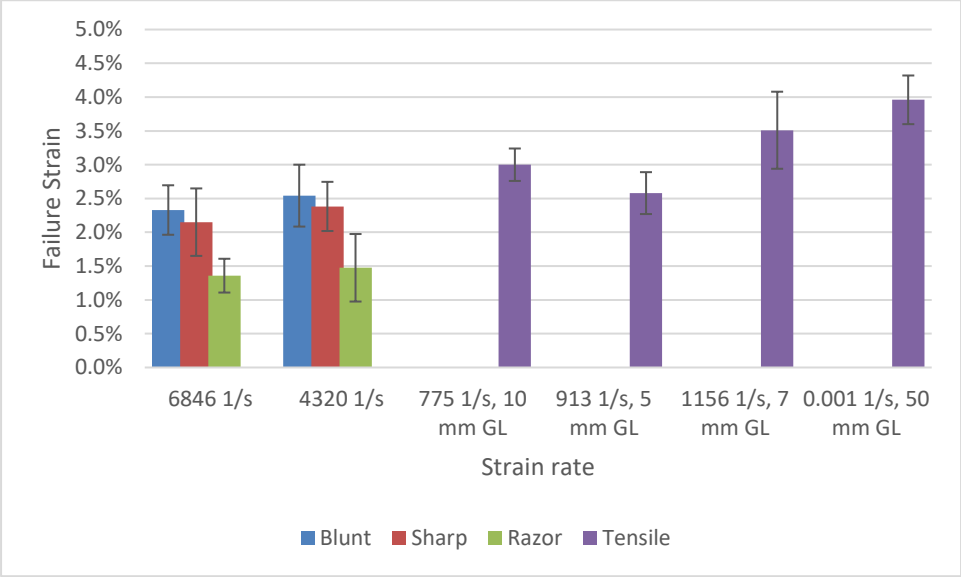

Figure 4.9 Average strain comparison with standard deviation

Table 4.1 Experimental Data Summary

Transverse Impact			**Velocity (m/s)**		**Strain Rate (s^{-1})**	**Strain (%)**		**Strength (GPa)**	
Geometry	**Speed**	**Sample Size**	**Avg.**	**S.D.**	**Avg.**	**Avg.**	**S.D**	**Avg.**	**S.D.**
Blunt	Fast	10	1.14	0.79	6951.2	2.33	0.37	4.15	0.70
	Slow	14	10.52	0.40	4369.2	2.54	0.46	4.50	0.75
Sharp	Fast	21	20.27	0.99	6796.9	2.15	0.50	3.91	0.63
	Slow	15	10.12	0.50	4285.0	2.38	0.36	4.40	0.60
Razor	Fast	10	20.24	0.69	6788.5	1.36	0.25	2.48	0.40
	Slow	16	9.86	0.41	4306.5	1.48	0.50	3.06	0.83
Tensile Data			**Gage Length (mm)**		**Strain Rate (s^{-1})**	**Strain (%)**		**Strength (GPa)**	
			Avg.		**Avg.**	**Avg.**	**S.D**	**Avg.**	**S.D.**
			10		775	3.00	0.24	4.08	0.17
			5		913	2.58	0.31	4.54	0.39
			7		1156	3.51	0.57	4.25	0.21
			50		0.001	3.96	0.36	3.69	0.17

For the blunt and sharp indenters, failure strain for the lower strain rate approaches failure strain for the HSR tensile results for the 5 mm gage length, where the razor is considerably lower compared to the blunt indenter (41.68% reduced at high rate and 41.98% reduced at low rate). Controlling for geometry, the slower strain rate demonstrates a mild improvement in strength, where the blunt has an 9.13% increase, the sharp has a 10.83% increase, and the razor has an 8.56% increase. Sharp indenters appear to have slightly reduced strength compared to blunt, with a 7.71% reduction at high rate and 6.27% reduction at low rate. Although the reduction is subtle, the presence of this trend in both the strength and failure strain indicates that it may represent a physical response rather than being mere sampling error.

Maximum angle of deflection is also recorded from the experimental images for correlation with data from Hudspeth et al. as depicted in Figure 4.10. Because the starting angle is 0° for all tests, the failure angle generally correlates with displacement and

therefore failure strain, but the blunt experiments notable show a smaller failure angle on average relative to the sharp experiments despite having a higher failure strain when controlled for strain rate. It is unknown whether this is a result of sampling error or reflective of a difference in some underlying failure mechanism.

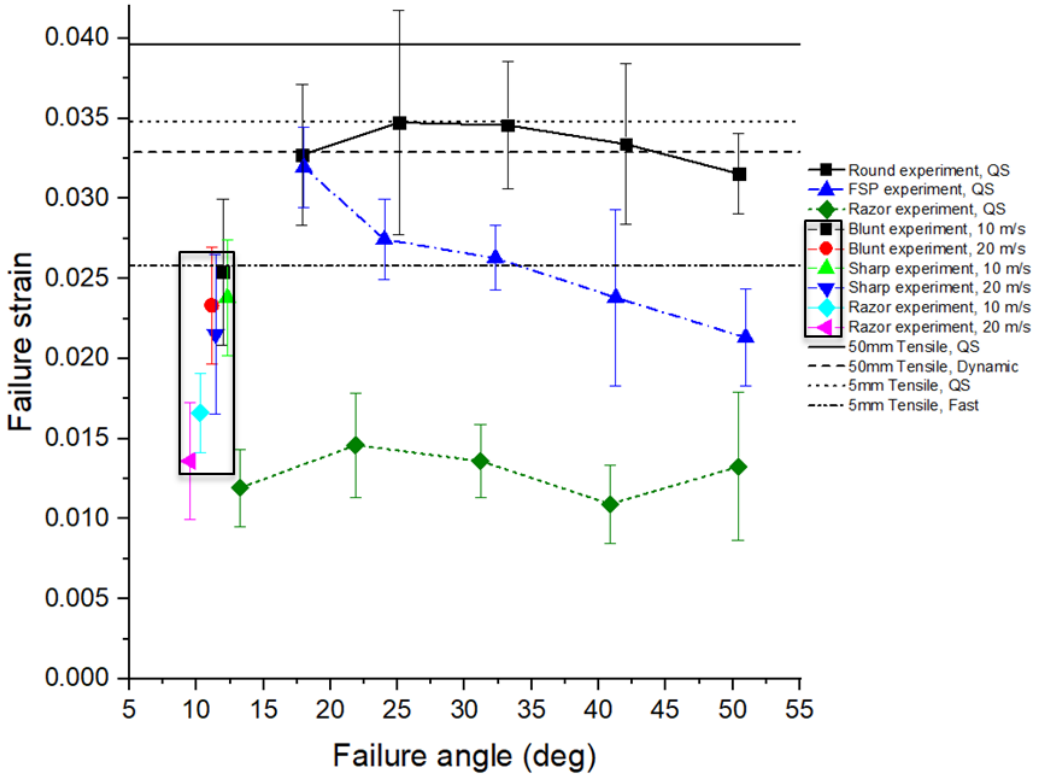

Figure 4.10 Strain as a function of failure angle. Additional data is from [11] and [21]. Horizontal lines represent tensile values, and values in box are from high-rate transverse impact.

As UHMWPE behaves linearly under HSR loading, the strength and failure strain can be used to estimate stiffness, which in turn correlates with the axial wave velocity. Based on the work of Cole et al., the impact velocity and axial wave velocity can be used to determine the transverse wave velocity as in Equation 2.1, and the initial angle can be calculated according to Equation 2.3 based on the work of Smith [4], [5]. Figure 4.11 plots these quantities over the full range of velocities experienced by ballistic materials using the

average effective modulus from experiments. Impact velocities in these experiments are relatively low and result in smaller wave angles and transverse wave speeds. Nominal strain rates as used in this study are obtained by dividing the transverse wave velocity by half the gage length (20.8 mm), as the loading is symmetric. These analytical quantities are calculated for each test, and the average values are included in Table 4.2.

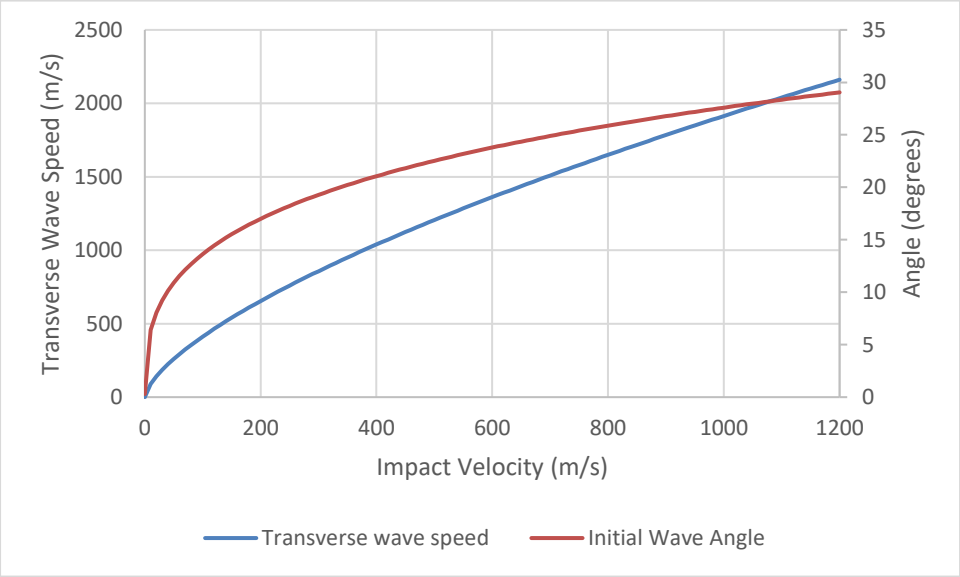

Figure 4.11 Transverse wave velocity and initial wave angle as a function of impact velocity

Table 4.2 Average and analytically determined properties

Geometry	**Blunt**		**Sharp**		**Razor**	
Strain Rate	**Fast**	**Slow**	**Fast**	**Slow**	**Fast**	**Slow**
Impact Velocity (m/s)	21.14	10.52	20.27	10.12	20.24	9.86
Effective Modulus (GPa)	180.1	180.7	186.1	186.1	185.0	215.7
Axial Wave Speed (m/s)	13581	13594	13811	13835	13780	14851
Transverse Wave Speed (m/s)	144.58	90.87	141.38	89.13	141.20	89.58
Strain Rate (s^{-1})	6951.2	4369.2	6796.9	4285.0	6788.5	4306.5
Initial Wave Angle (degrees)	8.32	6.61	8.16	6.48	8.16	6.28
Axial Wave Time (ms)	0.00153	0.00153	0.00151	0.00150	0.00151	0.00140
Transverse Wave Time (ms)	0.144	0.229	0.147	0.233	0.147	0.232
Time to Failure (ms)	0.213	0.447	0.212	0.451	0.169	0.359

Based on calculations, the time spent for the transverse wave from the impact to reach the end of the gage length (GL) on each side (TWT, calculated according to Equation 4.4) is close to halfway to time of failure, except in the case of fast razor loading, where the transverse wave travel time is relatively close to the failure time. Axial wave time (AWT) is calculated in the same way with the axial wave speed, as seen in Equation 4.5. Time scales for axial wave travel are very small relative to the overall time of the test. The short time scale for axial wave travel results in axial stress and strain being consistent in its increase due to wave reflections traveling quickly. However, other geometric behaviors are less consistent due to the slower wave propagation speed, resulting in other regions of strain concentration such as fiber kinking. This behavior is visible as the fiber exhibiting a "wobble" over time as it is displaced on video footage of experiments. For both axial and transverse waves, the presence of multiple wave reflections over the course of the

experiment results in calculations using Smith theory, which assumes an infinitely long fiber with no reflections, being inaccurate.

$$TWT = \frac{\frac{1}{2}GL}{c_s} \tag{4.4}$$

$$AWT = \frac{\frac{1}{2}GL}{c} \tag{4.5}$$

For blunt and sharp indenters, stiffness appears to be consistent between strain rates, despite the apparent strength reduction as strain rate increases. For the razor indenter, failure strain decreased more than strength as strain rate increased, resulting in the slower rate experiments having a higher apparent modulus. However, this data has relatively high variability, meaning this result could be a statistical artifact. High-rate stiffness values in Russell et al. are reported as being lower, and dynamic effects due to wave reflections at the fiber boundary could contributed to a higher apparent stiffness, but other factors in the previous study could also contribute to this difference. First, that portion of the study tests the tensile behavior of yarns, which underpredict stiffness and strength relative to equivalent tensile data. Additionally, the strain rates are reported as being approximately 10^{-3} s^{-1}, which may be reduced compared to strain rates observed in this research [12].

Several challenges have been encountered in the process of obtaining this data. First, because this experimental technique has not been used in the literature, no baseline data exists for verification purposes. Blunt impact data is fairly consistent across tests, but early sharp impact data shows smaller failure loads relative to the later data. Because the apparent strength seems to increase over time, efforts have been made to verify that no dulling of the sharp impactor has occurred, as well as production of new sharp indenters for comparison. After subsequent analysis, many of these early tests have been excluded based on other criteria such as insufficient velocity resulting in too small a strain rate.

Other difficulties relate to use of the photographic system. Insufficient light results in poor test recordings, and the high framerate compounds the issue because of the fast shutter speed. Additionally, determination of velocity and strain based on optical data is complex and error-prone due to the high potential for subjectivity. The maximum angle made by the fiber before failure is thought to be directly related to maximum strain, but the video data demonstrates that, although it is related, the angle is inconsistent over time due to wave reflections and repeated contact with the impactor causing the fiber to "bounce". This inconsistency is further demonstrated by the mismatch between failure angle and failure strain in Figure 4.10. Even so, the methods outlined above represent a critical and effective method for obtaining quantifying failure stress and strength in fibers under transverse impact.

4.2.3 Failure Surface Analysis

In order to compare failure mechanisms to existing literature, representative test samples are selected and examined under light microscope. Figure 4.12 presents images which demonstrate results similar to Hudspeth et al., where large-scale fibrillation is visible in the indenter with the largest loading radius, and the razor demonstrates significant shear failure. Like the FSP, the sharp indenter has macroscopic fibrillation, but a region where shear failure has occurred is also visible. Based on these observations, a 20 μm radius does induce some shear damage, but the effect on overall strength and failure strain is relatively minor.

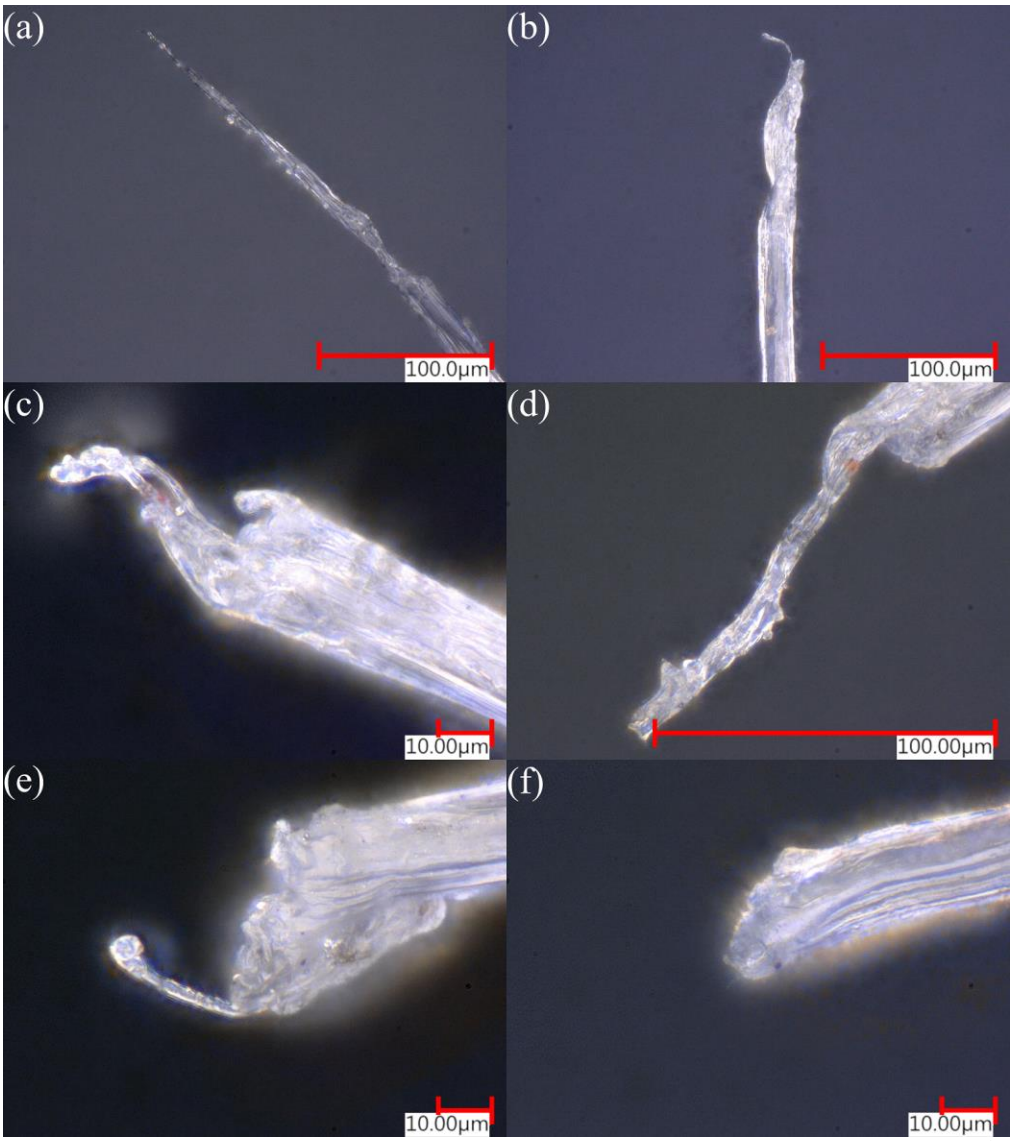

Figure 4.12 Broken fiber ends for each experimental case: (a) Blunt, 6951 s^{-1}; (b) Blunt, 4369 s^{-1}; (c) Sharp, 6797 s^{-1}; (d) Sharp, 4285 s^{-1}; (e) Razor, 6789 s^{-1}; (f) Razor, 4307 s^{-1}

4.3 SUMMARY

A new method for testing fibers for transverse impact strength and failure strain is presented. A Hopkinson bar is modified to launch loading geometry at a transversely mounted fiber, and load cells at the grips measure loads while a high-speed camera records macroscopic displacement and deformation over time. Tests are performed for 3 indenters with circular geometry of decreasing loading radius at two impact velocities resulting in

different strain rates. Strength values are consistent with tensile data, and strain values represent a significant reduction over tensile data as well as some QS transverse loading data, although razor indenters see a minor increase, most likely due to the sensitivity of the test to the starting angle, which is much lower relative to existing experimental data. Failure surfaces are consistent with the expected failure mechanisms, with fibrillation being dominant for larger loading radius and shearing being dominant for smaller loading radius. This consistent experimental data and methodology is necessary for model design and correlation, which should enable more detailed discussion of stress and strain conditions at the small length and time scales present in these loading conditions.

CHAPTER 5

FINITE ELEMENT APPROACH FOR SINGLE FIBER IMPACT

This chapter details the approach used to produce a finite element model replicating the experimental conditions as described in Chapter 4. An orthotropic material model is initially used to verify functionality of the mesh, boundary conditions, and general material properties, and a custom user-defined material model (UMAT) is used to improve accuracy at later loading stages.

5.1 ORTHOTROPIC MODEL DESIGN

5.1.1 Mesh Design

Because the loading is symmetric, a half model is used to save computational resources. A unit system consisting of mm, ms, kg, and kN is chosen, as those units best match the time and length scales of the experiment. Fiber gage length is 20.8 mm, equivalent to half the actual gage length of 41.6 mm. A representative fiber diameter of 0.0181 mm is chosen based on experimental measurements. Each indenter is modeled using sufficient elements to approximate the curvature while maintaining a reasonable computation time. Element size along the length is selectively refined to match the element size along the loading radius. A comparison of the different mesh designs can be seen in Figure 5.1.

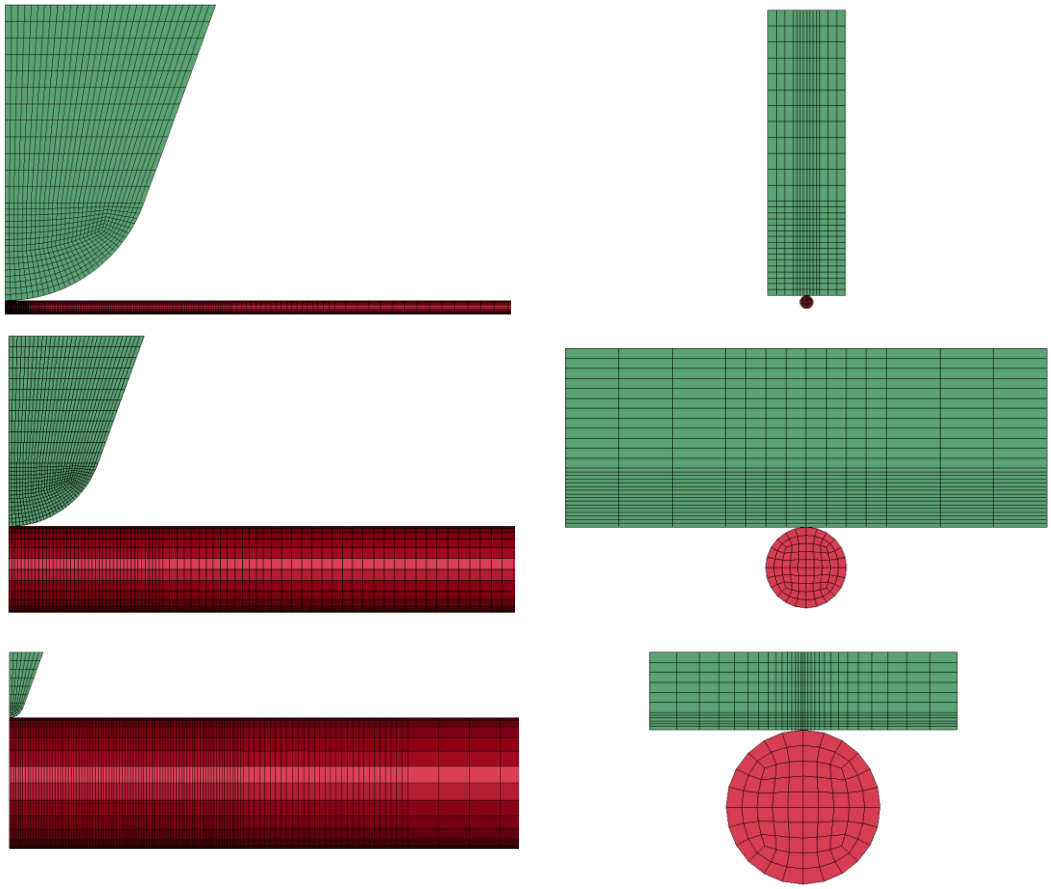

Figure 5.1 Front and side view of mesh for each model. From top to bottom: blunt, sharp, razor

5.1.2 Boundary Conditions and Input Properties

The boundary conditions used in this model are intended to accurately represent the actual testing conditions. Therefore, the nodes at the clamped end of the fiber gage area are constrained on all degrees of freedom. At the plane of symmetry, both the fiber and indenter have nodes constrained to prevent x displacement (parallel to the fiber direction) as well as rotation about the y and z axes. Single surface eroding contact is used to model the response of the fiber to impact by the indenter, and an initial velocity condition (either 10 or 20 m/s) is placed on the indenter.

The indenter is assigned a simple elastic material and given a standard Young's modulus and Poisson's ratio for steel, but the density is changed in order to match the mass

of the indenter and nylon sleeve (1.2865 g). Due to the dynamic nature of this model and the emphasis on the fiber, the need to match the mass outweighs any potential inaccuracy in material behavior within the indenter.

The fiber gage length is modeled using a simple orthotropic material and given properties from [25], which can be seen in Table 5.1. The fiber direction is assigned direction 3, with the impact direction being direction 1. Key elements and nodes are selected for extraction of high-rate binary data, and cross section planes are created for the reporting of forces traveling along the fiber.

Table 5.1 Initial input properties

ρ (g/cm^3)	d (μm)	$E_{1,2}$ (GPa)	E_3 (GPa)	G_{12} (GPa)	$G_{23,31}$ (GPa)	ν_{21}	$\nu_{31,32}$
0.97	18.1	1.0	116.0	0.357	3.0	0.4	0.6

This simple orthotropic model is sufficient to model early behavior such as initial indenter contact and strain wave propagation. However, it has a few shortcomings: First, the input properties are for quasi-static loading, where rate-dependent stiffening is most likely present due to the high strain rates, so loads are likely to be underpredicted. This can be addressed by replacing the axial stiffness with experimental apparent stiffness values. Second, the material model does not replicate the inelastic behavior of UHMWPE under transverse compression, so nonphysical behavior and numerical instability are observed at higher strain levels. To address this problem, the material model can be modified to incorporate this inelastic behavior from experimental characterization by means of a user-defined material model (UMAT).

5.2 UMAT APPLICATION

5.2.1 Implementation

The UMAT used in [16] and [25] was modified and compiled to run on the author's supercomputing cluster solution for running MPP-DYNA. Figure 5.2 presents the loading curve required for the material model to replicate the yielding behavior in transverse compression. Models utilizing the UMAT demonstrate significantly improved stability in late stage loading, making them useful for quantifying behavior at or near the point of experimental failure.

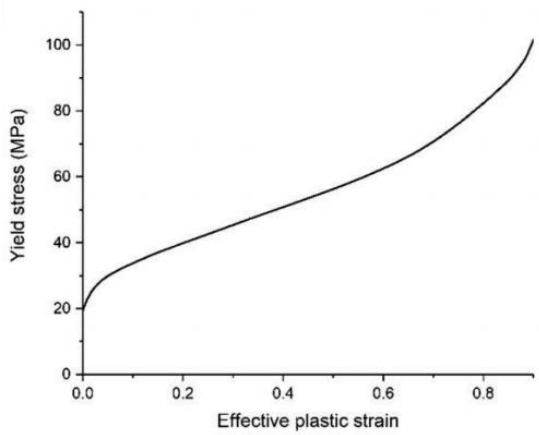

Figure 5.2 UMAT behavior under transverse compression [25]

5.2.2 Outcomes

Models contain approximately 61000-72000 elements and run with termination times between 0.18 ms and 4.7 ms on 30 processors. Compute times ran from 20 hours for simpler models to several days for models with finer meshes and longer termination times.

5.3 EXPERIMENTAL CORRELATION

To compensate for the stiffness increase due to strain rate dependency, effective stiffness values from experimental data are used for E_3 as shown in Table 5.2 and all other properties are held constant. After obtaining completed models, postprocessing is

performed to identify certain aspects of the material behavior. For example, the wave angle is compared to the analytical value as well as the measurement at time of failure, and the model load at the edge of the model is compared to load cell data in Figure 5.3. The wave angle behavior over time is consistent with the relatively large time scale of transverse wave reflections predicted in analytical calculations as well as the visible fiber "wobble" in experimental recordings.

Table 5.2 Effective E_3 values used in models

Geometry	**Blunt**		**Sharp**		**Razor**	
Strain Rate	**Fast**	**Slow**	**Fast**	**Slow**	**Fast**	**Slow**
E_3 (GPa)	214.0	201.4	191.8	186.9	175.4	181.2

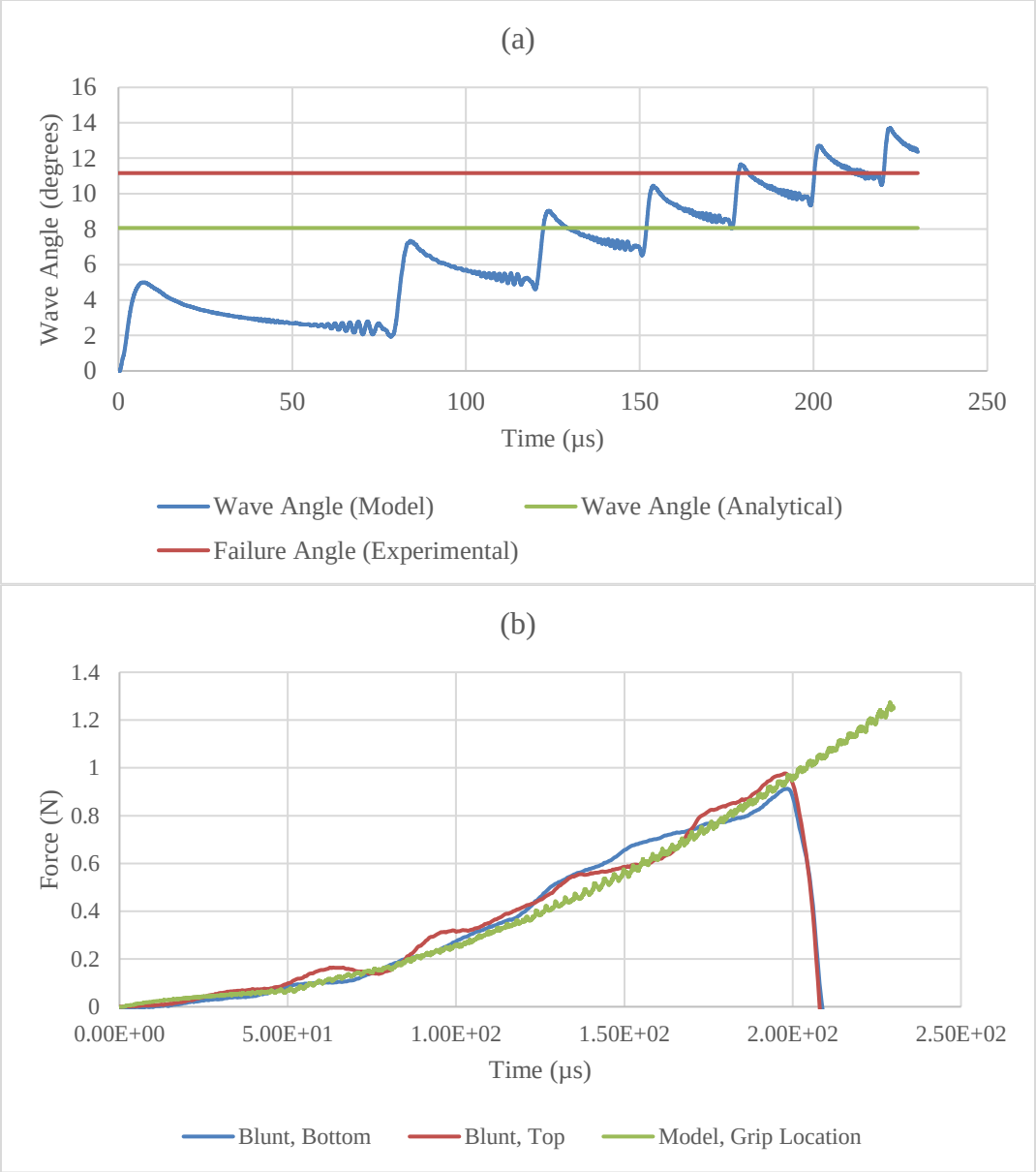

Figure 5.3 Model outputs correlated to analytical and experimental data for blunt, 6951 s^{-1} tests: (a) wave angle and (b) load cell data

Strain contours near the expected point of failure are analyzed for strain concentrations and other features. Some instability is observed at later time steps, but the data appears to be reasonable at time steps before the instability occurs. Figure 5.4, Figure 5.5, and Figure 5.6 present the axial strain on the 20 m/s models for blunt, sharp, and razor indenter geometry. Contours in blunt and sharp models are taken from 0.21 ms, which is immediately before the average failure time in the experimental data, and razor contours

are taken from 0.15 ms, as some nonphysical behavior begins to initiate after that point in the simulation. Strain is generally localized to the back side of the fiber, although the razor model is showing some concentration right beneath the indenter.

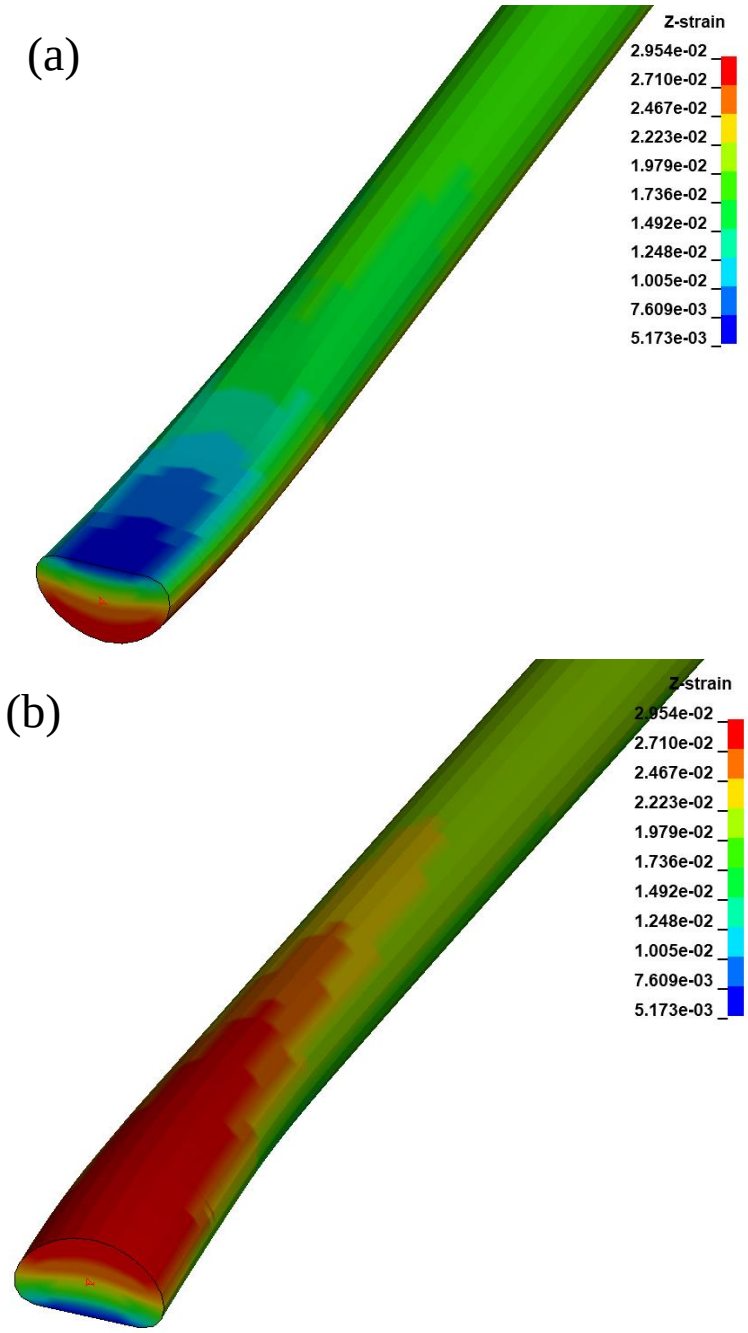

Figure 5.4 Axial strain contours for (a) front and (b) back surfaces of fiber impacted by blunt projectile at 20 m/s

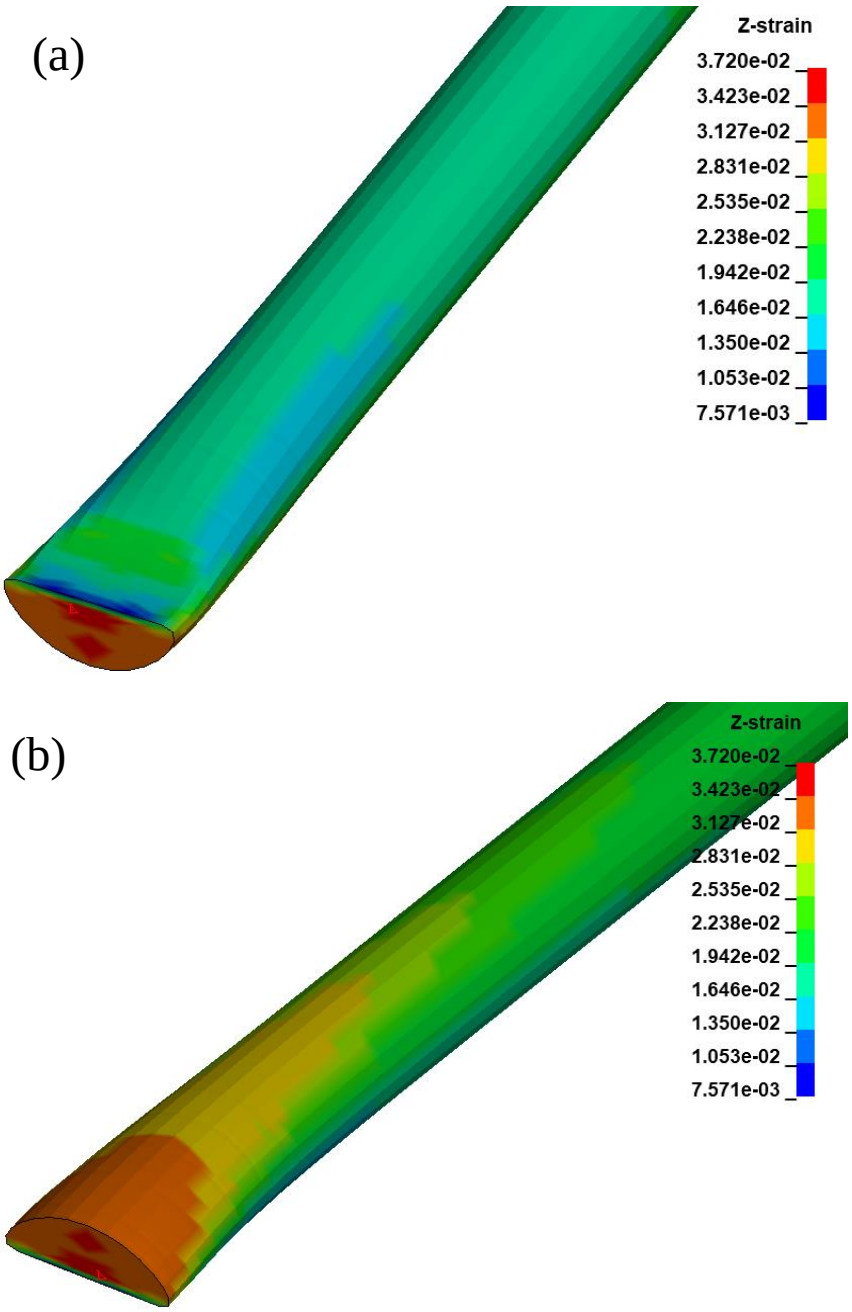

Figure 5.5 Axial strain contours for (a) front and (b) back surfaces of fiber impacted by sharp projectile at 20 m/s

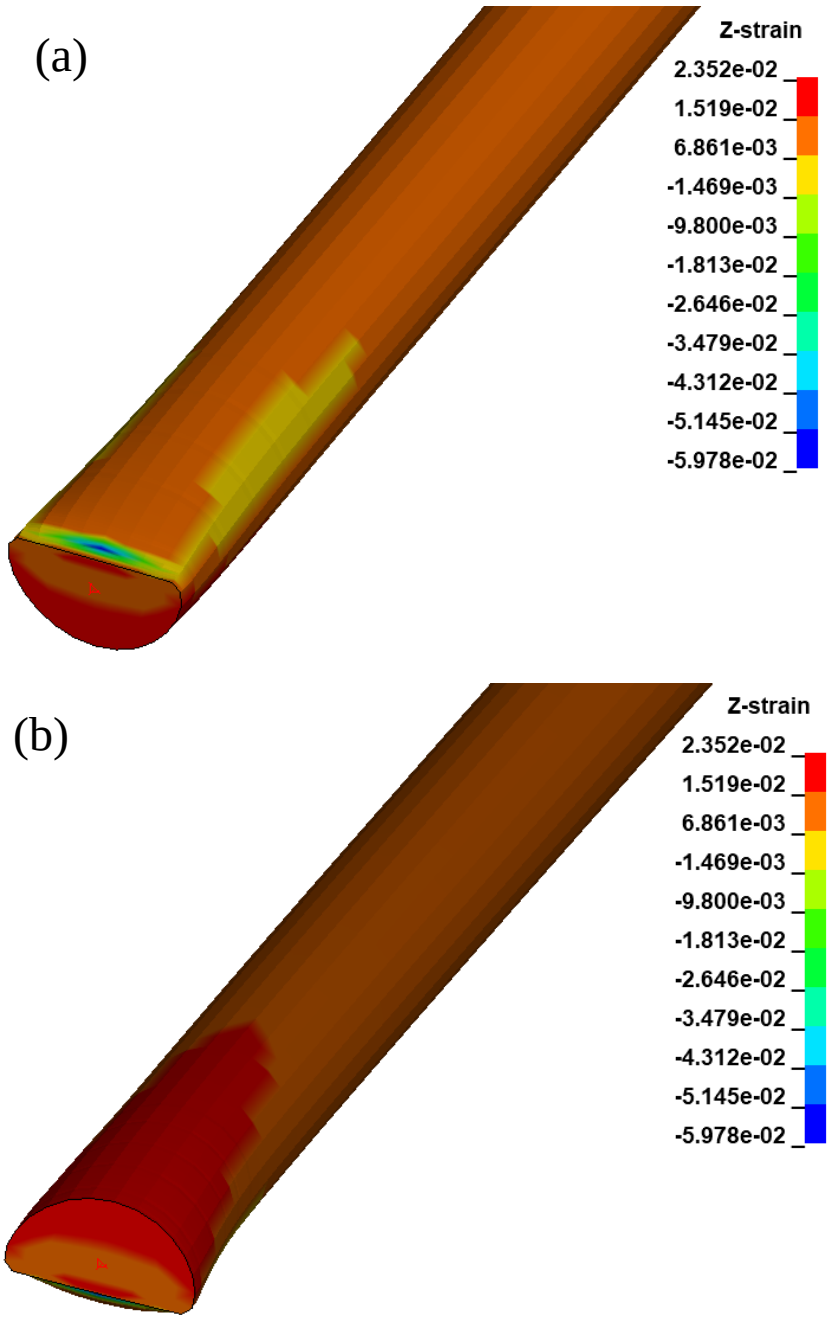

Figure 5.6 Axial strain contours for (a) front and (b) back surfaces of fiber impacted by razor projectile at 20 m/s

Significant transverse compression is observed in Figure 5.7, which indicates that strength reduction is occurring. Furthermore, transverse shear is especially prevalent in the sharp indenter in Figure 5.8. It is also present in the sharp indenter, and an interesting note is that the maximum shear stress is actually in the interior of the fiber rather than at the

surface. The blunt indenter shows transverse shear on the back face rather than the front face, but its magnitude is so small that it does not reduce the strain to failure in any meaningful sense. Contours have been obtained for the slow rate tests as well, but aside from slight differences in magnitude, the contours are not significantly different.

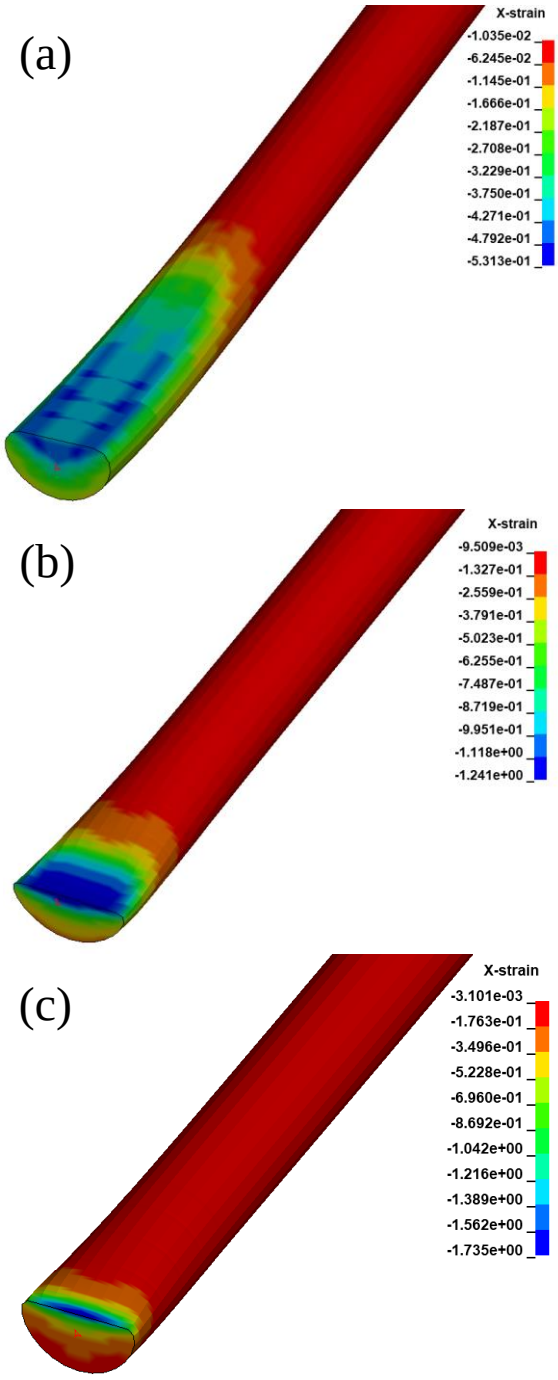

Figure 5.7 Transverse compression contours for (a) blunt, (b) sharp, and (c) razor indenters at 20 m/s

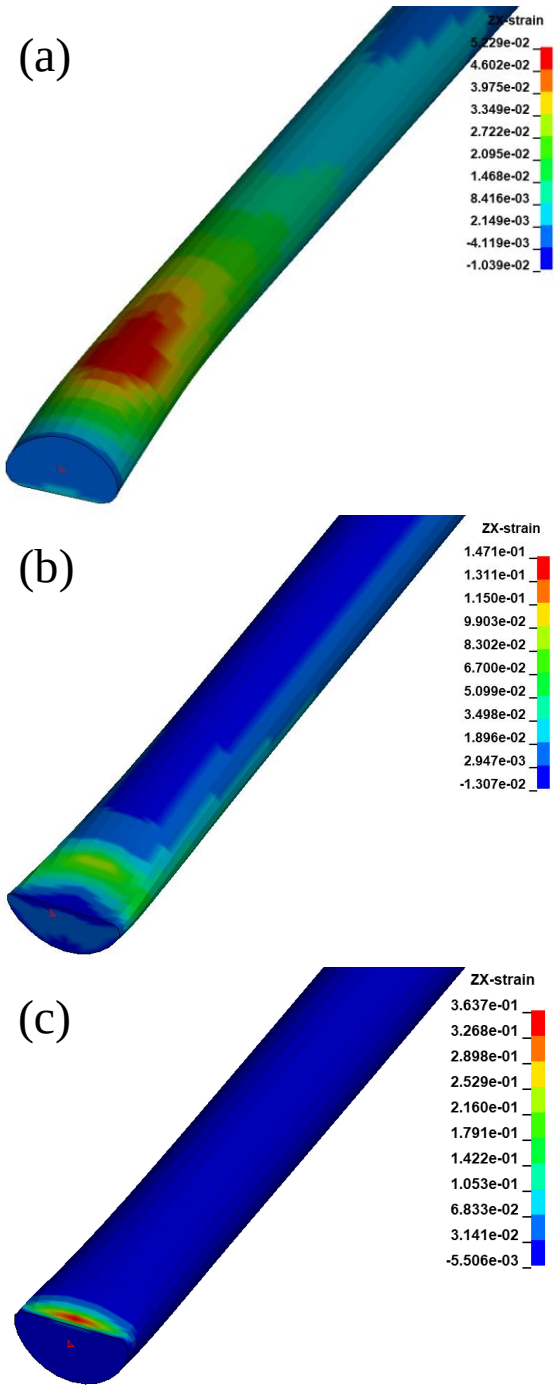

Figure 5.8 Transverse shear contours for (a) blunt, (b) sharp, and (c) razor indenters at 20 m/s

The region of axial stress concentration is measured from the models and incorporated into the Weibull probability model to predict the strain to failure for a sample with a gage length equivalent to the stress concentration region. The failure criterion formulation presented in Equation 2.4 is used, with the AC term set to zero, as axial compression is not expected to contribute to failure in this situation. TC terms are assumed to be 0.132 when transverse compression is present, SR terms are extrapolated from strain reduction seen in Sanborn et al.[11], and TS terms are based on the failure envelope in Hudspeth et al., which assumes that bending shear has a similar effect on axial strength compared to torsional shear [20]. Failure criterion inputs and values at the expected point of failure based on average strain levels are in Table 5.3, where average strain levels at the point of comparison are compared between experimental and model values. Contributions toward strength reduction from strain rate, axial compression, and transverse shear, which are plotted across applied axial strain for the sharp indenter at 6797 s^{-1} in Figure 5.10, and failure criteria values are plotted for all models in Figure 5.11. Blunt and sharp indenters come close to identifying failure but ultimately stop short, whereas the razor indenters predict failure much earlier than test results would suggest, resulting in a negative value at the expected point of failure. These results seem to indicate that more mechanisms are at work in fiber strength degradation, which makes further investigation necessary.

Table 5.3 Failure criterion inputs

Geometry	Blunt		Sharp		Razor	
Strain Rate	6951	4369	6797	4285	6789	4307
Average Axial Strain	0.0241	0.0251	0.0217	0.0235	0.0133	0.0148
Maximum Axial Strain	0.0336	0.0319	0.0335	0.0337	0.0301	0.0313
Strain Concentration Factor	1.39	1.27	1.54	1.42	2.26	2.12
Maximum Transverse Shear Strain	0.0806	0.0796	0.159	0.152	0.5329	0.548
L_C (mm)	0.33	0.28	0.09	0.15	0.13	0.11
$\varepsilon_3(L_c)$	0.0512	0.0518	0.0566	0.0543	0.0550	0.0556
TC	0.132	0.132	0.132	0.132	0.132	0.132
TS	0.000	0.000	0.037	0.029	4.301	4.720
SR	-0.194	-0.184	-0.194	-0.183	-0.194	-0.184
Output	0.937	0.870	0.878	0.893	-0.237	-0.213

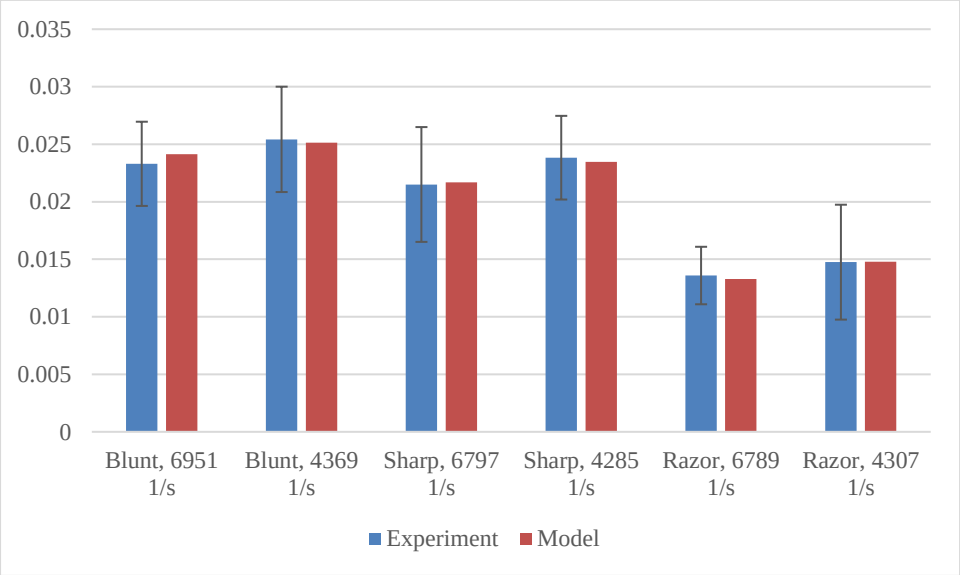

Figure 5.9 Strain values for use in failure criterion compared to experimental data

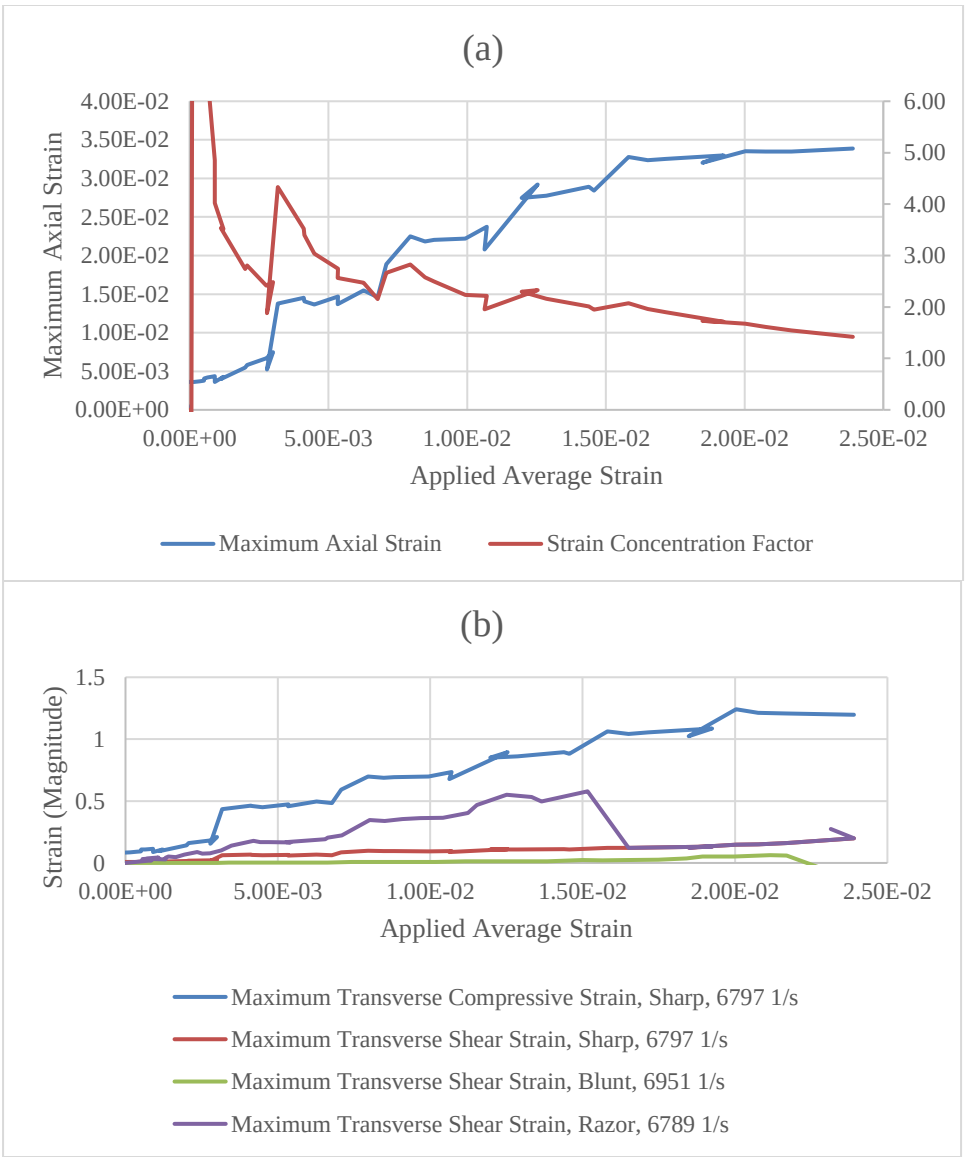

Figure 5.10 Failure criterion components for the sharp indenter at 6797 s^{-1}. (a) Maximum axial strain and strain concentration factor. (b) Transverse compressive and shear strains. Transverse compression is equivalent across all geometries, and transverse shear is comparable across strain rates.

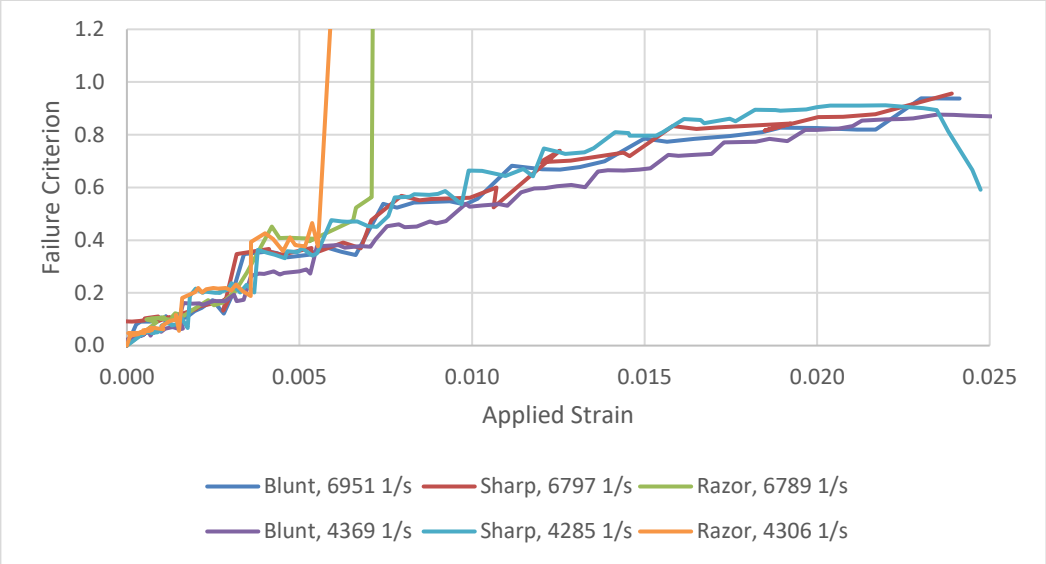

Figure 5.11 Failure criterion plots for all test groups

CHAPTER 6

CONCLUSIONS AND FUTURE WORK

In this thesis, a critical review of the existing body of literature concerning dynamic impact of high-performance ballistic fibers has been performed, which details previous efforts to quantify the dynamic behavior of single fibers for the purpose of predicting impact performance of woven fabric materials. A high-strain rate transverse compression technique is discussed, which results in a 19% decrease in strength at QS strain rates.

One notable experimental procedure which has not yet been described in literature is single fiber impact loading, although significant progress has been made through analytical and computational modeling for shaping expectations from such an experiment. In order to meet this need in material characterization, a novel single-fiber impact apparatus has been developed based on a small-diameter Hopkinson bar which uses load cell and high-framerate image data to obtain strength and failure strain in a transversely mounted fiber being impacted by a specified geometry. Loading geometries are all circular with varying radius including a razor (~2 μm), a sharp indenter (20 μm), and a blunt indenter (200 μm), and two impact velocities are chosen, 10 m/s and 20 m/s, which correlate to strain rates of approximately 4320 and 6846 s^{-1}.

Using this method, data has been successfully obtained for UHMWPE which correlates well with previous experimental efforts in other configurations. Failure strain for all groups is significantly reduced relative to existing tensile and quasi-static (QS) transverse loading data. For all the geometries, failure strains are reduced by 46-51%,

compared to QS tensile and 12-19% compared to QS transverse, as strain rates increased from 4320-6846 s^{-1}. Compared to high strain rate (1156 s^{-1}) tensile failure strain, significant reduction in failure strains are measured due to transverse impact loading. Failure strains (i) reduced by 28-34% for blunt impact at strain rates 4369-6952 s^{-1}; (ii) reduced by 32-39% for sharp impact at strain rates 4285-6797 s^{-1} and (iii) reduced by 58-61% for razor impact at strain rates 4307-6789 s^{-1}. For all the geometries, change in strength ranges from +6% to -2%, compared to QS tensile, as strain rates increased from 4320-6846 s^{-1}. Compared to high strain rate tensile strength, changes in strength can range from a slight increase to a significant reduction due to interactions between the rate-dependent increases in stiffness and strength, and strength degradation due to transverse loading. Strength measurements (i) range from +6% to -2% for blunt impact at strain rates 4369-6952 s^{-1}; (ii) range from +4% to -8% for sharp impact at strain rates 4285-6797 s^{-1} and (iii) range from -28% to -42% for razor impact at strain rates 4307-6789 s^{-1}. The reduction in tensile properties are attributed to the failure mechanism induced by different geometries. While all geometries induce axial compression due to the impact, the loading radius affects the degree of applied transverse shear, where little to no transverse shear is observed in the blunt indenter, an intermediate amount of shear is applied in the sharp indenter, and a high degree of shear is applied by the razor indenter. This conclusion is supported by failure surface images, where blunt impact results in fibrillation characteristic of tensile failure, razor impact results in fiber shearing characteristic of the cutting action of the razor, and the sharp impact demonstrates a mixed amount of both failure modes.

Previous modeling methods have been adapted for these dynamic loading conditions, and while many aspects of the output data correlate well to the experimental

results, some additional work is necessary in order for these methods to be useful in a predictive capacity.

Additionally, some improvements could be made to the experimental apparatus. The weakest components of the data gathering process are the lack of control over the velocity, as well as the difficulty in measuring the velocity. The current Hopkinson bar configuration is not robust enough to withstand a large range of applied pressure, which means the ability to change the impact velocity is limited until a more robust design is produced. Additionally, performing velocity measurements through image postprocessing carries some degree of uncertainty which could be mitigated by changing the setup to enable precise displacement measurements over time. For example, a laser-based system similar to the one used on many tensile Hopkinson bars could be set up, although the mobility of the nylon sleeve may still prove a challenge in terms of accuracy for such a system. Even so, the results seem reasonable and demonstrate great potential for this novel method of material characterization.

The techniques and concepts developed and applied in this work will be indispensable in growing the body of literature relating to single-fiber impact performance as well as in expanding the knowledge of similar materials. For doctoral work, the author intends to perform experimental characterization and model correlation of the interlaminar shear strength of UHMWPE film composites.

REFERENCES

[1] T. A. Stockdale *et al.*, "Hierarchical Mechanisms of Lateral Interactions in High-Performance Fibers," 2020, doi: 10.1021/acsami.9b23459.

[2] R. Marissen, "Design with Ultra Strong Polyethylene Fibers," *Mater. Sci. Appl.*, vol. 02, no. 05, pp. 319–330, 2011, doi: 10.4236/msa.2011.25042.

[3] R. Marissen, D. Duurkoop, H. Hoefnagels, and O. K. Bergsma, "Creep forming of high strength polyethylene fiber prepregs for the production of ballistic protection helmets," *Compos. Sci. Technol.*, vol. 70, no. 7, pp. 1184–1188, 2010, doi: https://doi.org/10.1016/j.compscitech.2010.03.003.

[4] J. D. Cole, C. B. Dougherty, and J. H. Huth, "Constant Strain Waves in Strings," *J Appl Mech*, vol. 20, pp. 53-SA-4, 1953, doi: 10.1017/CBO9781107415324.004.

[5] J. C. Smith, C. A. Fenstermaker, and P. J. Shouse, "Stress-Strain Relationships in Yarns Subjected to Rapid Impact Loading," *Text. Res. J.*, pp. 743–757, 1965, doi: 10.1520/stp47583s.

[6] D. Roylance, "Ballistics of Transversely Impacted Fibers," *Text. Res. J.*, vol. 47, no. 10, pp. 679–684, 1977, doi: 10.1177/004051757704701007.

[7] P. Cunniff, "Dimensionless Parameters for Optimization of Textile-Based Body Armor Systems," *Proceeding 18th Int. Symp. Ballist.*, no. January 1999, pp. 1303–1310, 1999.

[8] V. Sánchez-Gálvez, F. Gálvez, R. Sancho, and D. Cendón, “A new analytical model to simulate high-speed impact onto composite materials targets,” *Int. J. Impact Eng.*, vol. 108, pp. 322–333, 2017, doi: 10.1016/j.ijimpeng.2017.04.024.

[9] R. R. Ruiz, M. A. T. Galán, J. G. Carillo, and R. A. Gamboa, “Evaluation of Ultra High Molecular Weight Polyethylene (UHMWPE) anisotropic configuration sample of Tensylon™ , Dupont™ at medium velocity impact test,” *Mex. J. Mater. Sci. Eng.*, vol. 2, no. August, pp. 24–32, 2015.

[10] L. R. Vargas-Gonzalez and J. C. Gurganus, “Hybridized composite architecture for mitigation of non-penetrating ballistic trauma,” *Int. J. Impact Eng.*, vol. 86, pp. 295–306, 2015, doi: 10.1016/j.ijimpeng.2015.08.014.

[11] B. Sanborn, A. M. DiLeonardi, and T. Weerasooriya, “Tensile Properties of Dyneema SK76 Single Fibers at Multiple Loading Rates Using a Direct Gripping Method,” *J. Dyn. Behav. Mater.*, vol. 1, no. 1, pp. 4–14, 2015, doi: 10.1007/s40870-014-0001-3.

[12] B. P. Russell, K. Karthikeyan, V. S. Deshpande, and N. A. Fleck, “The high strain rate response of Ultra High Molecular-weight Polyethylene: From fibre to laminate,” *Int. J. Impact Eng.*, vol. 60, pp. 1–9, 2013, doi: 10.1016/j.ijimpeng.2013.03.010.

[13] M. Cheng, W. Chen, and T. Weerasooriya, “Experimental investigation of the transverse mechanical properties of a single Kevlar® KM2 fiber,” *Int. J. Solids Struct.*, vol. 41, no. 22–23, pp. 6215–6232, 2004, doi: 10.1016/j.ijsolstr.2004.05.016.

[14] S. Sockalingam, J. W. Gillespie, and M. Keefe, “On the transverse compression response of Kevlar KM2 using fiber-level finite element model,” *Int. J. Solids Struct.*, vol. 51, no. 13, pp. 2504–2517, 2014, doi: 10.1016/j.ijsolstr.2014.03.020.

[15] S. Sockalingam, J. W. Gillespie, and M. Keefe, “Dynamic modeling of Kevlar KM2 single fiber subjected to transverse impact,” *Int. J. Solids Struct.*, vol. 67–68, pp. 297–310, 2015, doi: 10.1016/j.ijsolstr.2015.04.031.

[16] S. Sockalingam, R. Bremble, J. W. Gillespie, and M. Keefe, “Transverse compression behavior of Kevlar KM2 single fiber,” *Compos. Part A Appl. Sci. Manuf.*, vol. 81, pp. 271–281, 2016, doi: 10.1016/j.compositesa.2015.11.032.

[17] S. Sockalingam, J. W. Gillespie, and M. Keefe, “Influence of multiaxial loading on the failure of Kevlar KM2 single fiber,” *Text. Res. J.*, p. 004051751668196, 2016, doi: 10.1177/0040517516681961.

[18] W. Weibull, “A Statistical Distribution Function of Wide applicability,” *J. Appl. Mech.*, vol. 103, pp. 293–297, 1951.

[19] S. Chowdhury, S. Sockalingam, and J. Gillespie, “Molecular Dynamics Modeling of the Effect of Axial and Transverse Compression on the Residual Tensile Properties of Ballistic Fiber,” *Fibers*, vol. 5, no. 1, 2017, doi: 10.3390/fib5010007.

[20] M. Hudspeth, X. Nie, and W. Chen, “Dynamic failure of Dyneema SK76 single fibers under biaxial shear/tension,” *Polymer (Guildf).*, vol. 53, no. 24, pp. 5568–5574, 2012, doi: 10.1016/j.polymer.2012.09.020.

[21] M. Hudspeth, D. Li, J. Spatola, W. Chen, and J. Zheng, “The effects of off-axis transverse deflection loading on the failure strain of various high-performance fibers,” *Text. Res. J.*, vol. 86, no. 9, pp. 897–910, 2015, doi: 10.1177/0040517515588262.

[22] J. H. Lee *et al.*, “High strain rate deformation of layered nanocomposites,” *Nat. Commun.*, vol. 3, no. May, 2012, doi: 10.1038/ncomms2166.

[23] D. T. Casem, S. E. Grunschel, and B. E. Schuster, “Normal and Transverse Displacement Interferometers Applied to Small Diameter Kolsky Bars,” *Exp. Mech.*, vol. 52, no. 2, pp. 173–184, 2012, doi: 10.1007/s11340-011-9524-x.

[24] F. D. Thomas, D. Casem, T. Weerasooriya, S. Sockalingam, and J. W. Gillespie, “Influence of high strain rate transverse compression on the tensile strength of polyethylene ballistic single fibers,” in *Conference Proceedings of the Society for Experimental Mechanics Series*, 2019, vol. 1, pp. 339–344, doi: 10.1007/978-3-319-95089-1_62.

[25] S. Sockalingam, F. D. Thomas, D. Casem, J. W. Gillespie, and T. Weerasooriya, “Failure of Dyneema® SK76 single fiber under multiaxial transverse loading,” *Text. Res. J.*, p. 004051751879865, 2018, doi: 10.1177/0040517518798653.